Technische Universiteit Delft

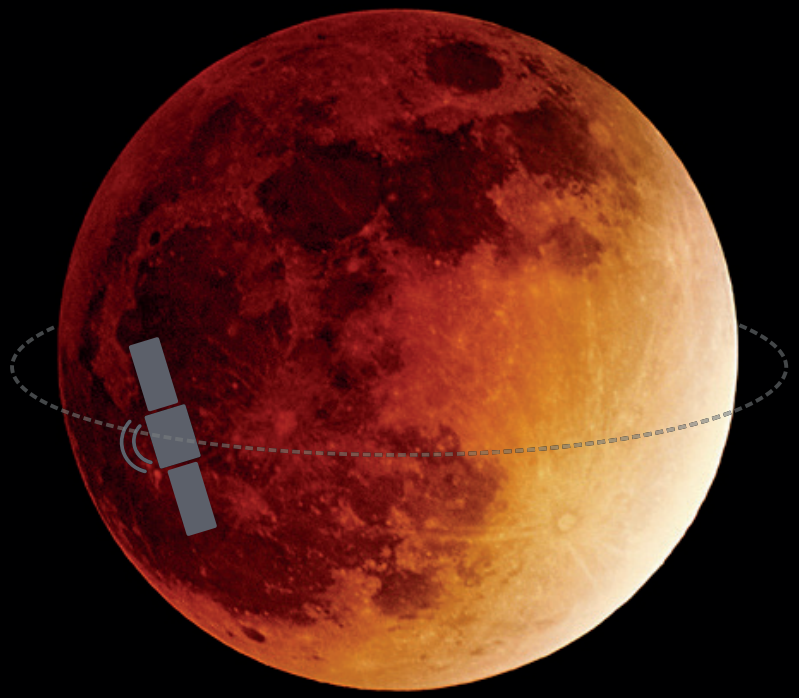

Assessment of Lunar Positioning Accuracy with PECMEO Navigation Satellites

M.A. Griffioen

TU Delft

Assessment of Lunar Positioning Accuracy with PECMEO Navigation Satellites

by

Mischa Adriaan Griffioen

to obtain the degree of Master of Science
at the Delft University of Technology,
to be defended on Thursday, February 20, 2020 at 9:30 AM.

Student number:	4377745	
Project duration:	March, 2019 – February, 2020	
Thesis committee:	Prof. dr. ir. P.N.A.M. Visser,	TU Delft, daily supervisor
	Dr. ir. E.J.O. Schrama,	TU Delft, committee chair
	Dr. J. Guo,	TU Delft
	Dr. M. Martin-Neira,	ESA ESTEC

An electronic version of this thesis is available at `http://repository.tudelft.nl/`.

TU Delft

Preface

With this document, I proudly present the research performed for my graduation, with the purpose of obtaining a degree of Master of Science in Aerospace Engineering. Besides many courses and an internship, it has been preceded by a literature study on the topic of Lunar navigation.

The work, as it is today, would not have been achieved without the help of several people. Firstly, I would like to acknowledge Manuel Martin-Neira, as the initiator of this research subject. I am very grateful for the feedback received during various meetings, as well as on written work, and providing me with ample information, sources and guidance where necessary.
Furthermore, I want to thank my thesis supervisor, Pieter Visser, whom not only gave me guidance on the process for both the literature study, the research, as well as writing this thesis, but also helped my shape my way of thinking about the research and its content. Surely, without him, this these would not be in the form that it is now, nor be of the quality that I consider it to be.

Finally, I applaud you, the reader, who picked up the work to read or study it. Without you, this document would not fulfill its ultimate purpose; passing on the information contained within.

M.A. Griffioen
Delft, February 2020

Abstract

Many low earth satellites use GNSS for orbit determination, both for operational purposes and post-facto scientific orbits. Using GNSS systems for Lunar navigation proves difficult, however, due to the signals being weak and having limited coverage. This thesis investigates, through numerical simulation, the usage of a constellation of Polar or Equatorial Medium Earth Orbit (PECMEO) satellites for Lunar navigation. The system is proposed as alternative for orbit determination using ground-based observations, making navigation of the spacecraft more autonomous, without limitations on the number of receivers.

A navigation constellation of 9 satellites at an orbital radius of 14 000 km is designed by minimizing the Geometric Dilution of Precision (GDOP). The resulting Pareto front of optimum solutions consists of two distinct groups of constellations. Firstly, constellation with lower mean GDOP and higher maximum GDOP have two orbits approximately orthogonal to the ecliptic plane, while the third orbit is in the ecliptic plane. Meanwhile, a second group of solutions with slightly higher mean GDOP, but significantly lower maximum GDOP are found for constellation with one plane approximately orthogonal to the ecliptic plane, while the remaining two planes have an inclination of near 45 degrees. One of the latter group of solutions has been chosen for the system for its lower maximum GDOP.

The effect of omitting observations passing through the ionosphere is investigated to determine if there is a need to obtain observations at multiple frequencies to allow for ionospheric corrections. Omitting those observations results in a slightly increased GDOP right before and after a satellite passes behind Earth, of up to 56.4%. However, only 13.9% of the samples are effected, making the overall effect rather small.

The positioning accuracy of the system is assessed by simulating pseudorange and carrier phase observations, and solving these with point position and kinematic least squares methods. Two main error contributions on the solutions are caused by observation noise and navigation satellite ephemerides errors.

A solution for observations without ephemeris error, a mean 3-dimensional position error of 3.3 m is obtained. A solution for noiseless observations yields a mean 3-dimensional position error of 26.8 m. Finally, the solution obtained from observations with all simulated errors results in a mean 3-dimensional position error of 27.0 m, to which the ephemeris errors are thus the main contributors, despite optimistic assumptions on their magnitude. The observed accuracy shows that the system is a viable navigation method for Lunar spacecraft.

Nomenclature

Symbols

δt	Clock error	s
δ	Kronecker symbol	–
ϵ	Observation error	m
γ	Eclipse angle	rad
γ	Time dilation factor	–
λ	Wavelength	m
μ	Standard gravitational parameter	$m^3 s^{-2}$
Ω	Right ascension of the ascending node	rad
ω	Argument of periapsis	rad
ϕ	Carrier phase	rad
ρ	Geometric range	m
σ	Standard deviation	
τ	Signal travel time	s
θ	Antenna main lobe half-angle	rad
θ	True anomaly	rad
$\vec{e}$	Eccentricity vector	–
$\vec{H}$	Orbit angular momentum vector	$m^2 s^{-1}$
$\vec{h}$	Modeled observations	m
$\vec{r}$	Least square residuals	m
$\vec{r}$	Position vector	m
$\vec{z}$	Observation vector	m
a	Semi-major axis	m
B	Bandwidth	Hz
B	Bias estimation parameter vector	m
b	Bias estimation parameter	m
c	Speed of light in a vacuum	$m s^{-1}$
C/N_0	Carrier-to-noise density	–
d	Early-to-late correlator spacing	–
E	Eccentric anomaly	rad

e	Eccentricity	–
e	Line of sight vector	–
f	Earth flattening factor	–
f	Frequency	Hz
G	Gain	–
H	Design matrix	–
H	Orbit angular momentum	$m^2 s^{-1}$
h	Time step size	s
i	Inclination	rad
k	Boltzmann constant	JK^{-1}
L_0	Free space loss	–
M	Mean anomaly	rad
M	Number of bias parameters	–
N	Integer ambiguity	–
N	Normal matrix	m^{-2}
N	Number of epochs	–
n	Mean motion	$rad s^{-1}$
P	Power	W
P	Pseudorange	m
Q	Covariance matrix	m^2
R	Radius	m
S	Bias term	m
SNR	Signal to noise ratio	–
T	Predetection integration interval	s
t	Time	s
T_E	Effective noise temperature	K
v	Velocity	$m s^{-1}$
W	Weight matrix	m^{-2}
X	State estimation parameter vector	m

Superscripts

ϕ	Carrier phase observation
b	Body
BB	Bias sub-matrix
BX	Bias-state sub-matrix

c	Clock
c	Coverage
E	Earth
i	Epoch index
i	Light time effect iteration step
j	Bias index
k	Observation index
M	Moon
N	Noise
n	Nominal
PR	Pseudorange observation
r	Receiving satellite
S	Signal
t	Transmitting antenna
XB	State-bias sub-matrix
XX	State sub-matrix

Subscripts

eq	Equatorial
po	Polar
s	Navigation satellite

Abbreviations

BDS	BeiDou Navigation Satellite System
C/A	Coarse/Acquisition
DOP	Dilution of Precision
DSN	Deep Space Network
ECI	Earth Centered Inertial
EIRP	Effective Isotropic Radiated Power
GDOP	Geometric Dilution of Precision
GNSS	Global Navigation Satellite System
GPS	Global Positioning System
IRNSS	Indian Regional Navigation Satellite System
LEO	Low Earth Orbit
LOC	Limit of Coverage
LOLA	Lunar Orbiter Laser Altimeter

LRO Lunar Reconnaissance Orbiter

LSQ Least Squares

LuNNaC Lunar Near-side Navigation Constellation

MEO Medium Earth Orbit

MOEA Multiobjective Evolutionary Algorithm

NASA National Aeronautics and Space Administration

PDI Powered Descent Initialization

PECMEO Polar or Equatorial Circular Medium Earth Orbit

PRN Pseudorandom Noise

RSS Root Sum Square

SSD Sample Standard Deviation

UERE User Equivalent Range Error

Contents

1 Introduction

After the end of the US *Apollo* program in 1972 and the the Soviet *Luna* program in 1976, the popularity of the Moon as spaceflight destination saw a sharp decline. In the decades that followed, only a handful of spacecraft entered the Lunar gravity well with the purpose to stay. The recent years, however, once again saw numerous launches of robotic missions to the Moon, with many more planned. Moreover, various countries, including China, India, Japan, the USA, and Russia have plans for manned missions to the moon. Another major goal is the Lunar Gateway, an international effort to build a space station in Lunar orbit.
Many technological improvements since the 1970s enable these new space missions. Highly efficient electric propulsion will be used for orbit maintenance on the Lunar gateway. Flight computers have become much smaller and more powerful, with many CubeSats having greater processing capacity and more memory than the Apollo flight computer.
Similarly, after the deployment of the first GPS satellites, its benefit to navigation in low Earth orbit was realized quickly as well, with Landsat-4 carrying the first GPS receiver into Low Earth Orbit. The low power and mass requirements for GNSS receivers, combined with their accuracy makes them broadly applicable. Furthermore, as the satellite solves the navigation solution on-board, there is no need to continuously track the satellite and upload navigation data from the ground, potentially reducing operation infrastructure complexity and cost. Besides real-time navigation, this technology has been adapted for clock synchronization and post-facto orbit determination on many satellites. However, due to its low transmission power, Earth nadir pointing, and the large signal travel distance, orbit determination using GNSS proves difficult in Lunar orbit.
This thesis proposes a new constellation of Earth orbiting navigation satellites to be used for in Lunar and cislunar navigation; LuNNaC, the *Lunar Near-side Navigation Constellation*. The system is to deploy satellites in a Polar Equatorial Medium Earth Orbit (PECMEO), as proposed by Martin-Neira et al. [2017]. Such a PECMEO constellation will consist of three orthogonal orbital planes, such as the example shown in Figure 1.1. This thesis investigates the technical performance of such a system, to investigate the feasibility and competitiveness compared to other Lunar navigation methods.
The subsequent section will elaborate the research objectives for this work. Furthermore, the research questions will be stated. For the research, navigation observations have been simulated, and solved using navigation techniques. The set up of this simulation tool will be explained to provide the reader with a framework which can be used to see how various parts of the thesis fit together. Finally, this chapter will conclude with an ouline of how the thesis is structured.

1.1. Research objectives and motivation

In order to advance the human exploration of extraterrestrial bodies, it seems that indeed an effort has to be made to advance the navigation abilities near the Moon. The ultimate goal of LuNNaC is to boost Lunar exploration by providing improved and inexpensive navigation solutions. Reducing complexity of navigation, and simultaneously improving navigation solutions can overall yield a boost for the Lunar spaceflight industry, ensuring rapid technology and scientific progress.
The objective of this research work is to investigate the technical performance of using PECMEO satellites for Lunar navigation. This is to give insight into the benefits of such a system with respect to its alternatives,

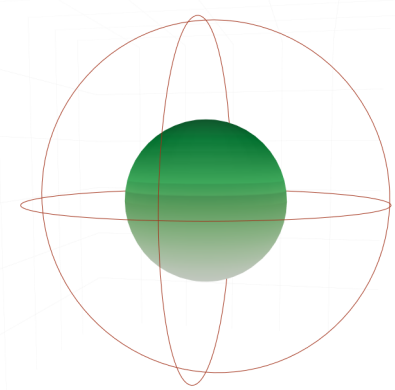

Figure 1.1: Orbits of a PECMEO constellation.

to see if further investigation is desired, and where this effort should then be focused. This is defined by the main research question for this thesis:

What is the real-time Lunar navigation accuracy when making use of PECMEO navigation satellites?

Various aspects of this question require further explanation. Firstly, Lunar navigation accuracy is considered the accuracy of the position determination of a spacecraft in Lunar orbit for operational purposes, such as orbit corrections. Furthermore, the real-time aspect for the navigation is considered a constraint to the use of (near) real-time ephemerides, rather than precise, post-facto ephemerides. In contrast, for the purpose of this research, on-board capabilities and limitations in processing of the receiving spacecraft will not be considered for the design of navigation algorithms.
Naturally, the orbits of the navigation satellites will impact the quality of the navigation solution. As no design of such orbits has taken place, the first step in this thesis is to perform this design. Optimal orbits will need to be found in order to ensure that no pessimistic insight into overall performance will be given. This yields the following sub-question:

What PECMEO constellation results in the best Lunar navigation geometry?

Performing numerical optimization of the navigation geometry will answer this question. Provisionally, that is, because only a small number of constraints will be considered here, whereas, when such a design project progresses, surely more constraints will be introduced. For the purpose of this research, only this initial optimization will be considered, as the entire iterative design is too large of a process to be captured in a single thesis.
The next step in the research is to apply the constellation that has been found, and simulate corresponding observations. After processing these results in a navigation algorithm, the difference between position solution and true orbit defines the navigation error. When no errors have been induced on the observations, one can expect to obtain no navigation error. On these observations, measurement errors due to thermal noise can be added. When compared to regular GNSS observations, the signals need to travel a much larger distance, which results in a large signal attenuation, and therefore larger observation errors. This rises the following research question:

What is the magnitude of Lunar navigation error induced by thermal measurement noise?

Besides thermal noise, the accuracy of the ephemeris will influence the accuracy of the navigation solutions. This influence is investigated with this question:

What is the magnitude of Lunar navigation error induced by errors in the navigation satellite ephemerides?

With the LuNNaC system, the received navigation signals only travel through the ionosphere when a navigation satellite is close to its eclipse behind Earth, as seen from the receiver. This gives rise to the opportunity to neglect observations with an ionospheric delay in order to not require multi-frequency systems, which increase complexity. The effect of omitting these observations is assumed to be small with respect to corrected observations, which is tested along the following question:
What is the effect of neglecting ionospherically delayed observations on the navigation solution?

Finally, improved navigation solutions are not only of interest to spacecraft in Lunar orbit. When transferring from an Earth orbit to a Lunar orbit, as on a trans-Lunar trajectory, and vice versa, the orbit of a spacecraft needs to be monitored closely to perform the right injection manoeuvres, or corrections to have correct reentry conditions. Therefore, the following question is to evaluate the use of LuNNaC in trans-Lunar or trans-Earth trajectory:

Can the PECMEO satellites be used for navigation in a trans-lunar orbit?

Answers to these questions are to give insight into the technical performance of PECMEO satellites for Lunar navigation. Comparing this technical performance to requirements and performance of alternatives will allow a first evaluation of the feasibility and competitiveness of the system. Finally, recommendations can be given for research to either develop the system further, or directions where enhancement of its performance is most likely.

1.2. Overview of Lunar Navigation Simulator

For the purpose of this research a Lunar Navigation Simulator has been developed to numerically find navigation accuracy of a LuNNaC receiver in Lunar orbit. In order to understand how several discussed effects and models fit together, one should first understand the general overview of the entire simulation performed. Although partly intertwined, four stages can be distinguished, as displayed in Figure 1.2.
Firstly, an orbit evaluation stage is used to find states, consisting of position and velocity for satellites at given times. This is used for both the transmitter satellite states and the receiver states, the output of which is used to simulate observations, as well as a reference as correct receiver positions, which would be the perfect navigation solution.
The second stage is the *signal simulator*. Here, propagation of clock errors take place, and satellite states are used to simulated observations performed by a LuNNaC receiver through observation equations. Furthermore, errors on the observations are induced here, and erroneous ephemerides are generated based on the true transmitter orbits.
These observations are used in the third stage of the simulation. Firstly, an apriori solution is created using a point position least squares method. Afterwards, a Kinematic least squares method is used to improve the solution further by combining the pseudorange with the carrier phase observations. From this, solutions for the receiver positions and clock errors are obtained.
Finally, in a post-processing, or accuracy determination stage, the obtained solutions can be compared to the 'true' input values as given by the propagator stage to determine the positioning performance of the system.

1.3. Outline

Now that the general research subject, objectives and method have been clarified, this section is used to familiarize the reader with how this document is layed out.
The concept for the use of PECMEO as Lunar navigation constellation is further elaborated in chapter 2. Furthermore, some general assumptions on the implementation of the system will be elaborated. This includes assumptions on the ephemeris errors. Finally, this chapter will show some competitive systems for Lunar navigation and their accuracy, to highlight the desired level of accuracy for a Lunar navigation system.
The first step to simulating navigation measurements, is to determine reference states and clocks for both navigation satellites and the receiver. Therefore, chapter 3 defines the reference frames worked with in this thesis. It is shown how the clock (error) propagation is performed, and interpolated upon to determine the inertial time of observation epochs. Furthermore, two reference orbits used for creating results are shown in this chapter.

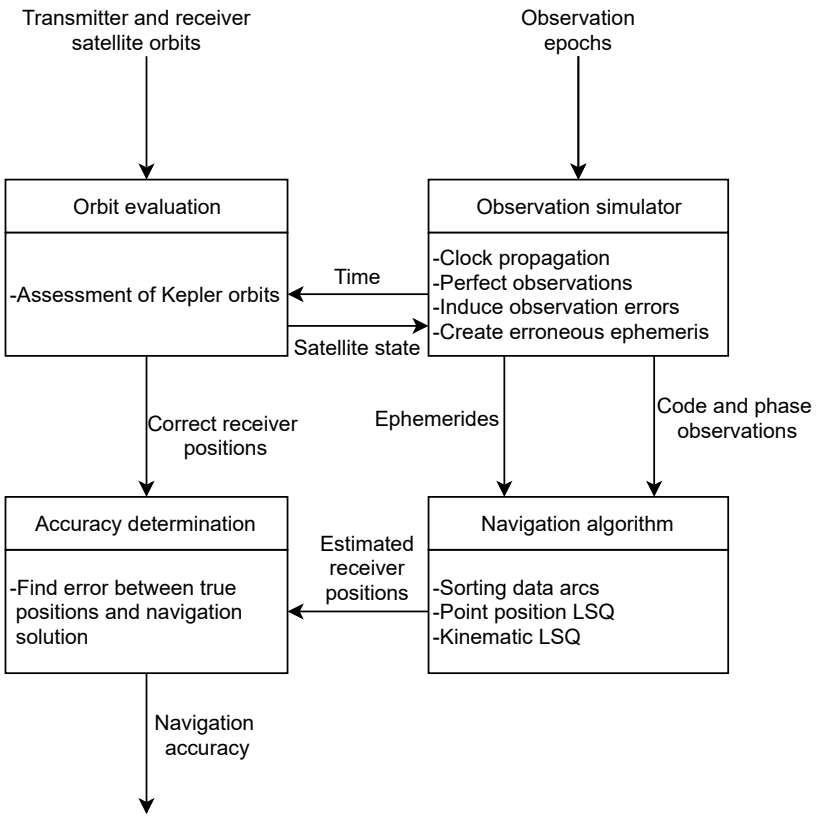

Figure 1.2: The four steps in the simulation of navigation solutions.

Chapter 4 elaborates on the various observations used for the navigation system. This includes the observation equations and various effects on the signals. For example, the Moon and Earth occasionally block the path for a signal, preventing it to reach the receiver. Moreover, thermal noise on the observations will be elaborated, and it is shown how this effect is modeled using the link budget of the system.
Based on navigation geometry, an initial optimization of the constellation, with the resulting design is presented in chapter 5. Furthermore, various design assumptions are explained, as well as the optimization objectives and used method.
Measurements are combined through navigation algorithms to form a navigation solution. The implemented point positioning and kinematic least squares methods are elaborated in chapter 6. Furthermore, the obtained solutions when applying these methods will be shown.
The conclusions from this research project are given in chapter 7. Furthermore, various suggestions are made on how research can and should be continued after this project.
Finally, several appendices give a summary of additional information, that does deserve a place in this document. Firstly, Appendix A summarizes various constants used throughout the research. Appendix B presents a table of the Kepler elements of the individual LuNNaC satellites as obtained through the optimization. Furthermore, Appendix C presents the created implementation of Kepler orbit in the Julia programming language, and its performed verification. In Appendix D, the software used during the research project is summarized.

2

PECMEO for Lunar navigation

This chapter will introduce the LuNNaC concept, along with some of the assumptions made on the implementation. Firstly, the concept of the system is introduced, with an explanation on some of the design decisions on the usage of some of the fundamental technologies for the system, such as the use of one-way ranging, and the application of GNSS to the system. Furthermore, various assumptions on the system will be presented, especially with respect to signal specifications and ephemerides. Finally, a few alternative systems for Lunar navigation are presented. This will allow LuNNaC to be compared to these systems to see how LuNNaC is of additional value, and to compare their performances.

2.1. LuNNaC

The LuNNaC system is based on the technological principles of GNSS; using navigation satellites to transmit the navigation signals, allowing receivers to perform one-way ranging, based on these signals. The satellites of the navigation constellation are positioned in medium Earth orbits, allowing those satellites to determine their orbits using GNSS observations. More specifically, the navigation satellites are placed in a PECMEO constellation, which consists of three orthogonal orbital planes. Such a configuration is presumed to have a high up time fraction when the line of sight to the Moon is clear, as well as provide a relatively good navigation geometry in comparison to other orbital plane configurations.

2.1.1. One-way ranging: multiple access and on-board processing

One of the major factors that enables the wide-spread use of GNSS systems is its multiple access feature, meaning that many users can use it simultaneously. This is achieved by making the satellites only transmit a generalized navigation signal to a broad direction. Determining the position of a receiver can be done directly by listing to those messages, and determining their timing, without the need for anything receiver specific or a reply. Therefore, a GNSS system can be used by anyone with a device capable of receiving the signals without degrading the system performance, removing the limit on the number of users. Whereas on Earth, every new cellphone, car or LEO satellite can determine their position using GNSS, the multiple access of LuNNaC will enable an inexpensive navigation solution for every communication satellite, capsule or rover around or on the Moon.

This scaling is one of the opportunities of LuNNaC; although a large upfront investment is required, it will be future-proof by supporting any number of synchronous Moon missions. In contrast, ground stations receive signals from satellites from which they determine their position. This requires the ground station to listen to such a satellite specifically, and therefore is not capable of tracking a large number of them in a parallel and continuous fashion. Hence, GNSS style one-way ranging is deemed the best ranging technique for such a system.

Furthermore, GNSS techniques are based on receiving devices capable of calculating a navigation solution on-board. For example, car navigation can be used without relying on external servers and/or services, by merely using the GNSS signals. Therefore, one can autonomously - without depending on an external party - find their current position. Similarly, using the GNSS one-way ranging techniques for navigation of spacecraft allows for a higher level of autonomy of the spacecraft when compared to other ranging techniques.

Such autonomy is highly beneficial in Lunar spaceflight as well for three reasons: Firstly, less operators are

Table 2.1: Orbits of various GNSS constellations. Orbital period have been obtained from Montenbruck et al. [2015].

Constellation	Orbit type	Inclination	Orbital period	Satellite altitude
GPS	MEO	55°	11h 58m	20 200
GLONASS	MEO	65°	11h 16m	19 100
Galileo	MEO	56°	14h 05m	23 200
BeiDou-2	MEO	55°	12h 53m	21 500
	IGSO	55°	23h 56m	35 800
	GEO	0°	23h 56m	35 800
IRNSS	IGSO	29°	23h 56m	35 800
	GEO	0°	23h 56m	35 800

needed for a highly autonomous satellite, reducing its operation cost. This will make the production of commercial infrastructure, such as Lunar communication satellites, more attractive. Moreover, the number of points of failure can be reduced, as the system is less dependent on external factors, and the entire chain of obtaining a navigation solution is shorter. Finally, as highlighted by Christian and Lightsey [2009], the requirements for the Orion spacecraft dictate that the vehicle must be able to return to Earth without contact to Earth. When an appropriate receiver would be incorporated in the spacecraft, this requirement could be fulfilled with the LuNNaC system. With the use of LuNNaC, a Lunar mission does not require a communications link to Earth to determine its trajectory accurate enough for the return to Earth. Moreover, the obtained solution is not dependent on a human factor. During the Apollo missions, an optical sextant could be used to re-configure the flight computer, as shown by Hoag [1969]. More recently, as shown by Holt and Wood [2019], test have been conducted on board of the International Space Station using a handheld sextant, which is meant as emergency navigation on board of Orion exploration missions. Therefore, implementation of LuNNaC enables the spacecraft to safely return to Earth without contact to a ground station, while not depending on observations that are prone to human errors. Hence, cost of Lunar exploration can be reduced, while reliability and human safety is improved with the use of LuNNaC.

2.1.2. Usage of GNSS for ephemeris generation

The LuNNaC navigation satellites can use GNSS systems for accurate and reliable determination of their orbits. Usage of inter-satellite ranging is to further enhance the accuracy of these ephemerides, and obtain a very low error level close to real-time. Generally, GNSS navigation geometry and signal reception is best at altitudes well below the GNSS satellites, as elaborated by Moreau et al. [2000]. As seen in Table 2.1, GLONASS satellites are located in the lowest orbits of the various GNSS systems at 19 100 km altitude. In order to make optimal use of the GNSS signals, the LuNNaC satellites are to positioned below this altitude, at an orbital radius of 14 000 km.

2.2. Assumptions on implementation

For the purpose of this thesis, many technical properties will be based on existing GNSS technology. Hence, several assumptions on how the system is implemented and on how it works are made. Here, these assumptions are explicated and quantified.

2.2.1. Signal specifications

For the LuNNaC signal, the GPS L1 signal is assumed with the C/A code. Therefore, the carrier frequency is 1575.42 MHz, hence the carrier wavelength $\lambda = 0.1903$ m. Using a similar frequency to GPS gives the advantage that the correlation between thermal noise and signal strength, derived for GPS, will be valid for LuNNaC when in the correct range of signal strengths.

For the navigation code signal the C/A chip length of 293 m is used. Shorter chips, such as 29.3 m for the P(Y) code will yield more accurate pseudorange observations. However, these will also require longer PRN code lengths. In comparison, C/A has a code length of 1023, L1C has 10230, and the P(Y) code has 6.19×10^{12}. A shorter code length will result in a shorter time to first fix, as the right correlation is more simple to find. When in lunar orbit, loss of lock to all satellites can occur quite frequently, when passing on the far side of the moon, and thus it is desirable to have a fast fix to satellites. Moreover, due to the use of phase measurements, the pseudorange accuracy does not have a large influence on the achievable position knowledge accuracy.

2.2.2. Signal transmission

For LuNNaC the navigation signal is transmitted through a high gain antenna, which is continuously aimed towards the Moon. In order to be used for a large variety of Lunar missions, the coverage of LuNNac is extended up to the edges of the Moon's Hill sphere, which has a radius of 61.5×10^6 m. Considering a transmitter on a point in its orbits closest to the Moon, the required beam half-angle is 9.6°. Adding a margin for pointing precision of the transmitting satellites, the main lobe will have a half-angle of 10°. This beam half-angle can be found through Equation 2.1. In the equation r_c represents the radius used for coverage around the body, where the Hill sphere radius is used. Furthermore, r_m is the Earth-Moon distance, and r_t is the orbital radius of the transmitter.

$$\tan\theta = \frac{r_c}{\sqrt{(r_m - r_t)^2 - r_c^2}} \tag{2.1}$$

The need for this large angle is emphasized by the possible orbits for NASA's gateway space station, seen in Foust [2019]. A distant retrograde orbit at 70.000 km above the Lunar surface, or a near-rectilinear halo orbit, with a maximum altitude of 75.000 km are amongst the options for the orbit for this station. Either of these orbits will be partly outside of the main lobe when designing for satellites within the Hill sphere.
The half-angle required for a GPS satellite to cover the entire earth is 13.9°, as shown by Moreau et al. [2000]. This angle would be 12.4° for GALILEO. The LOC (limit of coverage) for GALILEO is given at 12.67° as per Montesano et al. [2007]. Therefore, the antenna for LuNNaC can have a higher gain than these antennas. As a simplification the LuNNaC transmitter antennas are assumed to radiate isotropically in their main lobe, and no side-lobes are assumed. For this constant gain, the maximum gain of the GALILEO antenna is used, which is approximately 16.5 dB, which is a linear gain of 44.7.
A real transmitting antenna must have a mean gain lower than 1, in order for the total input power to be smaller than the total output power. The equation of the relative area of a spherical cap, with respect to the full sphere is given by $\frac{1}{2}(1-\cos\theta)$. Multiplying this by the constant gain for this angle will yield the mean gain when considering only the main lobe, which is approximately 0.34. Hence, about a third of the power used by the antenna will be transmitted towards the Hill sphere of the moon.
Considering the minimum gain at LOC for Galileo to be 15.35 dB, thus the power fraction transmitted in the main lobe is at least 0.42. In comparison, the antenna gain for LuNNaC can thus be said to be rather conservative.

Besides gain, the input power will have large effect on the received power of the signal. For this, a value of 119 W is used, which is equal to the power transmitted in the E1 band by GALILEO satellite E209 as shown by Steigenberger et al. [2018].
Together, gain and power can be used to find EIRP, effective isotropic radiated power. EIRP represents the transmitted power as observed by a receiver under the assumption that the same power is transmitted into a single direction. Hence, it is a representation for transmitted power as observed by a receiver. EIRP is calculated according to Equation 2.2.

$$EIRP = G_t \cdot P_t \tag{2.2}$$

In this equation, G_t is the dimensionless transmitter antenna gain. P_t is the power transmitted by the transmitting antenna.

2.2.3. LuNNaC ephemeris accuracy

The ephemerides of the navigation satellites is used to find the positions of these satellites at desired times while obtaining the navigation solutions. As this study limits itself to Kepler orbits, ephemerides are assumed to be in Kepler elements as well, quite similar to the broadcast ephemeris of GPS and Galileo. For a given satellite, the ephemeris will be assumed to be updated every 30 minutes and consist of discrete sections of Kepler orbits starting from each update time.
The ephemeris for the LuNNaC satellites is obtained through two types of observations. Firstly, the navigation satellites themselves will make use of various existing GNSS systems for both pseudorange and carrier phase observations. Moreover, precise intersatellite ranging within the navigation constellation is to further enhance the position knowledge of these satellites. With this combination, it is expected that centimeter level ephemeris accuracy is achievable on a near real-time basis. However, the true achievable accuracy of the ephemerides is not subject to this study.

Ephemeris errors are induced upon the true Kepler orbits of the navigation satellites in three directions; one radial, a prograde and an out-of-orbital-plane component. An equal accuracy level, ϵ_e is assumed for each of these components. The ephemerides are created by taking the presumed real orbit for the navigation satellite right at the start of the desired valid time span for this ephemeris, and modifying the Kepler elements. The error in radial direction is induced on the semi-major axis. The standard deviation for this component is $\sigma_a = \epsilon_e$. Furthermore, the second error component in the orbital plane is obtained through the anomaly, where its standard deviation is $\sigma_\theta = \frac{1}{a}\epsilon_e$ [radian]. When applying a given change along these two Kepler elements, the position of the satellite in its orbit does not influence the RSS position error in the ephemeris. For the out-of-plane component, however, such an influence is present, as a change in inclination has a most strong effect at the points furthest away from the x-y reference plane and follows a sinusoidal pattern, with orbital period as period of the oscillation.. The magnitude of the standard deviation is modified as to get the absolute mean error on the right level, hence it becomes $\sigma_i = \frac{\sqrt{2}}{a}\epsilon_e$ [radian]. As a result, the error at the ascending and descending node of the orbit will remain zero, but the expected error at the extreme z-positions is amplified.
The second major out-of-plane effect, the right ascension of the ascending node, is not used for inducing an ephemeris error as its effect is not limited to a single plane. Rather, the effect of an error in this element gives a combination of prograde and out-of-orbital-plane error based on the inclination of the orbit. The error is purely along the former direction with $i = 0$, while purely along the latter in a polar orbit.
Each of these Keplerian error components are assumed to be distributed normally with a mean at 0 m. The accuracy on each component is assumed to be 0.01 m. Hence, the standard deviations for the Kepler elements become, respectively, 0.01 m, 7.143×10^{-10} rad, and 1.010×10^{-9} rad for the semi-major axis, true anomaly and obit inclination.

A Monte Carlo analysis is applied to find the magnitude of the initial 3-dimensional (3D) position errors. In total, 10 000 samples are used, for which a semi-major axis, true anomaly and inclination error is generated. The same errors are then applied at 100 different, equally spaced, locations in the orbit in order to eliminate effects that are dependent on the orbital phase. Initially, the anomaly is changed to achieve the desired phase, after which the Kepler errors are applied. The three Cartesian error components and their RSS are now obtained, by comparing the Cartesian position before and after applying the Kepler errors.
Table 2.2 shows the empirical means and sample standard deviations for the numerical results of this Monte Carlo simulation performed for each of the thee PECMEO orbits. From the inputs, it can be seen that the obtained sample standard deviations from the randomly generated numbers are within 1 % to their desired values. Moreover, the mean Kepler errors are, with respect to their standard deviation, close to zero. As a result, the obtained Cartesian errors components have a mean near zero, with a standard deviation of approximately 0.01 m, which verifies the method used to translate the Cartesian accuracy into corresponding Kepler errors. The mean 3d position error is for all orbits approximately 1.57 cm with an 1.0 cm accuracy on all components. The sample standard deviation (SSD) for the RSS error is approximately 7.3 mm.

A similar experiment is repeated to find the ephemeris errors before an update occurs, as the position errors will change due to orbital motion. For this, both orbits before and after application of errors in the Kepler elements are propagated for 30 minutes and their Cartesian elements are compared. These simulations are based solely on Kepler orbits, hence an effect of orbit perturbations on ephemeris accuracy is not investigated.
The results for this experiment are found in Table 2.3. After the ephemeris error has propagated for 30 minutes, the empirical mean for the 3d position error has increased to approximately 1.78 cm for all orbital planes, with an SSD of around 9.4 mm. This increase in both mean error and standard deviation means that, in general, the accuracy of the ephemeris will worsen over time. The cause of this can be found in the adaptation of the orbital period of the ephemeris when a semi-major axis error is induced, which induces a time dependent error in the orbit anomaly. Although the anomaly error can give an initial offset, resulting in the total RSS error first decreasing before increasing again due to this time dependent effect, the first derivative of the RSS error with respect to time is always positive when considering short time spans with respect to the orbital period for the relative phase between the two orbits, which explains the increase in ephemeris error over time. Moreover, the position error due to inclination error will also change when propagating the orbit, as this position error is dependent on the position of the spacecraft in its orbit respect to the ascending node. For a circular orbit, however, this effect will result in an increasing error for the two

Table 2.2: Monte Carlo results for initial ephemeris errors. Shown are the sample standard deviations and empirical means of the numerical results.

Orbital plane		Input parameters			Results			
		Δa [m]	$\Delta\theta$ [rad]	Δi [rad] l	Δx [m]	Δy [m]	Δz [m]	RSS error [m]
Plane 1	μ	4.693×10^{-5}	-4.632×10^{-12}	2.120×10^{-11}	-3.417×10^{-7}	3.217×10^{-7}	6.484×10^{-7}	0.015 75
	σ	1.0086×10^{-2}	7.1497×10^{-10}	1.0129×10^{-9}	1.0021×10^{-2}	1.0005×10^{-2}	1.0047×10^{-2}	7.3173×10^{-3}
Plane 2	μ	-1.564×10^{-4}	-6.460×10^{-12}	-7.371×10^{-12}	9.344×10^{-7}	2.1473×10^{-7}	1.6384×10^{-6}	0.015 73
	σ	1.0008×10^{-2}	7.1974×10^{-10}	1.0081×10^{-9}	1.0036×10^{-2}	9.9688×10^{-3}	1.0041×10^{-2}	7.3233×10^{-3}
Plane 3	μ	1.5832×10^{-5}	8.4728×10^{-12}	-8.6375×10^{-12}	-8.553×10^{-7}	1.813×10^{-6}	1.1315×10^{-6}	0.015 66
	σ	9.998×10^{-3}	7.107×10^{-10}	1.0029×10^{-9}	9.975×10^{-3}	9.971×10^{-3}	9.975×10^{-3}	7.2892×10^{-3}

Table 2.3: Monte Carlo results for ephemeris errors at the end of its valid range, right before an update occurs. Shown are the sample standard deviations and empirical means of the numerical results.

Orbital plane		Input parameters			Results			
		Δa [m]	$\Delta\theta$ [rad]	Δi [rad]	Δx [m]	Δy [m]	Δz [m]	RSS error [m]
Plane 1	μ	1.696×10^{-4}	-1.060×10^{-11}	-2.848×10^{-14}	-2.486×10^{-6}	2.257×10^{-6}	1.424×10^{-6}	0.017 82
	σ	1.0060×10^{-2}	7.0853×10^{-10}	1.0120×10^{-9}	1.1476×10^{-2}	1.1030×10^{-2}	1.2299×10^{-2}	9.3309×10^{-3}
Plane 2	μ	-3.375×10^{-5}	-3.208×10^{-12}	-3.260×10^{-12}	-1.511×10^{-7}	-3.297×10^{-7}	1.737×10^{-7}	0.017 84
	σ	9.9904×10^{-3}	7.0876×10^{-10}	1.0089×10^{-9}	1.1781×10^{-2}	1.1876×10^{-2}	1.1281×10^{-2}	9.4340×10^{-3}
Plane 3	μ	7.181×10^{-5}	-6.414×10^{-12}	-8.086×10^{-12}	-1.197×10^{-6}	9.827×10^{-7}	-9.789×10^{-7}	0.017 77
	σ	1.0038×10^{-2}	7.0789×10^{-10}	1.0145×10^{-9}	1.1733×10^{-2}	1.1812×10^{-2}	1.1224×10^{-2}	9.3464×10^{-3}

quarter orbit sections directly after the ascending and descending nodes, while decreasing the position error in the two sections before these nodes, and therefore its mean contribution to the ephemeris error after propagation is zero. Finally, the SSD of individual Cartesian components have also increased by 10 to 19 percent towards the end of the 30 minute validity interval of the ephemeris when compared with the values at the start of the interval.

2.3. Navigation alternatives

Multiple options for navigation in Lunar orbit currently already exist or are being currently developed. For the LuNNaC navigation system to be of any use, it should have added value over these existing systems. Here, several alternative navigation methods will be explained. Furthermore, a prediction of their navigation precision will be given, which can be used later on for a quantitative comparison to the LuNNaC precision. Moreover, the navigation methods will be compared qualitatively to LuNNaC, to see what the advantages and disadvantages of the alternatives are with respect to LuNNaC.
Aforemost, it should be mentioned that of the discussed systems, LuNNaC is likely to require the largest upfront investment to develop, manufacture and operate satellites specific for lunar navigation.

2.3.1. Groundstation based ranging

Historically, navigation of a satellite in transfer to, and in orbit around the Moon has been performed using ground tracking. In order to perform this task, multiple ground stations around the world need to be available for tracking. Moreover, these stations can only track a small number of satellites at a time, hence, when increasing the number of satellites in Lunar orbit, the infrastructure must be improved drastically.
Table 2.4 shows the estimation position and velocity error for the navigation used for various burns in the Apollo 10 mission as presented in D'Souza et al. [2007]. These authors argue that the real-time tracking capabilities for the Orion capsule en-route to the moon will be comparable to these values, due to more advanced technology but a lesser tracking geometry. It shows that, for real-time position determination, the estimated magnitude of position errors was well above 1 km, and could even exceed 10 km. Hence, achieving a precision in the order of magnitude of 1 km can be considered acceptable for such missions..
Moreover, Mikrin et al. [2010] mention an expected position accuracy when using NASA's Deep Space Network (DSN) of 10 m.

Table 2.4: Estimated position error of the Apollo 10 mission, at various moments just before several burns, as shown in D'Souza et al. [2007].

Error component	LOI 1	LOI 2	LOI 3
Radial (U) [m]	924.15	157.28	924.15
Downrange (V) [m]	1539.55	5487.01	1539.55
Crossrange (W) [m]	2471.62	13890.04	2471.62
Total	3055.02	14935.37	3055.02
Radial Rate (U-dot) [m/s]	0.9879	0.0043	0.9879
Downrange Rate (V-dot) [m/s]	0.3587	0.1045	0.3587
Crossrange Rate (W-dot) [m/s]	2.225	0.3078	2.225
Total	2.461	0.325	2.461

2.3.2. Terrain relative navigation

Terrain relative navigation works by using surface features of a body and correlating these to a known database of such features. Several of such options exist. Firstly, optical imagery can be used to distinguish various features, such as Lunar craters can be recognized directly, or by their cast shadows. Similarly, some terrain relief can be recovered from the shadows casted from hills and surface features. Moreover, one can use techniques to recognize the contour of the Moon from a photograph of the horizon, and recover the position of the camera from that, as described in Mikrin et al. [2010]. Another example, Bilodeau et al. [2014] proposes a system for recognizing surface features to accurately estimated position and velocity for a Lunar lander. They report a position error of approximately 230 m at Powered Descent Initialization (PDI), at an altitude of approximately 10 km, while the accuracy reduces to below 10 m in the Powered Descent (PD) of the Lunar lander. Hence, optical terrain relative navigation methods can yield a rather high position accuracy at low altitudes. However, the accuracy decreases with increasing altitude. Moreover, these optical

instruments can only function in the day side of the Moon with proper lighting conditions.

Terrain relative navigation can also use other techniques besides image processing techniques. Another option for terrain relative navigation is the usage of altimetry using radar or LIDAR instruments. This has the advantage of being completely independent of lighting conditions. For example, the Lunar Reconnaissance Orbiter carried the Lunar Orbiter Laser Altimeter (LOLA) instrument (Yu et al. [2011]). Mazarico et al. [2012] propose to use crossovers in the laser data to enhance the position determination of the satellite. However, Mazarico et al. [2017] concluded that the benefit of the inclusion of these data was too marginal in comparison to the added complexity of the model to be of added value. Therefore, these data were abandoned for the purpose of orbit determination in this study.

3

Orbit simulation and clock propagation

Simulating the navigation process using LuNNac around the Moon requires position knowledge of both the navigation satellites and the receiving spacecraft. Therefore, orbit simulations are performed. This chapter discusses the reference frames used for the orbit simulation, and briefly discusses the orbit simulation itself. Moreover, simulation of satellite clock errors, caused by relativistic effects are discussed. Finally, the reference orbits for the receiving spacecraft used in the complete navigation simulation are presented.

3.1. Reference frame definitions

Throughout the simulations, an Earth centered inertial (ECI) reference frame is assumed. Furthermore, the global coordinate system has three ortogonal axis, where the x-axis point towards the mean equinox, the z-axis points along the celestial north pole, and the y-axis is orthogonal to both x and z in a fashion that results in a right-handed coordinate frame.

Moreover, inclinations of Earth orbiting objects are described as inclined from the mean ecliptic.
In order to be able to identify relative observed time, as described in section 3.3, a time reference is introduced as follows: A stationary observer in the described ECI frame, at an infinite distance from the reference frame center, hence, were no gravitational attraction is experienced, is assumed to be "inertial time". This "inertial time" is assumed to propagate at a constant rate and is used as a reference to describe the progression of time for other observers.

3.2. Satellite state propagation

For satellite state propagation, only Keplerian orbits have been used. Therefore, all gravity sources are described by point masses. In the simulations, a satellite is only attracted by the body that applies the dominant acceleration. The equations and methods used for Keplerian orbit calculations can be found in Appendix C, in combination with the verification of the method.

3.3. Relativistic clock dilation

Clocks on board of spacecraft are subject to two different relativistic effects. Firstly, in accordance with general relativity, a clock closer to a gravitational body appears to tick faster than one that is further away from the same body. Secondly, when compared to a static observer, moving clocks will seem to tick slower than the static clock, as per Special Relativity.
It should be noted, however, when considering an Earth-centered inertial (ECI) reference frame, with a uniform Earth gravity field, both time dilation effects are a constant effect on the clock frequency for a satellite in circular Earth orbit, as both its gravity potential and velocity remain constant. As a result, both effects can be compensated by adjusting the pre-launch progression rate of the clock. For the purpose of this research, this is assumed to be done for the PECMEO navigation satellites, for which, as a result, no time dilation effects are determined.
When considering a receiver clock in low circular Lunar orbit, one can assume the gravitational potential to be constant, with the gravity of the Moon being the dominant term. Hence, the gravity time dilation is

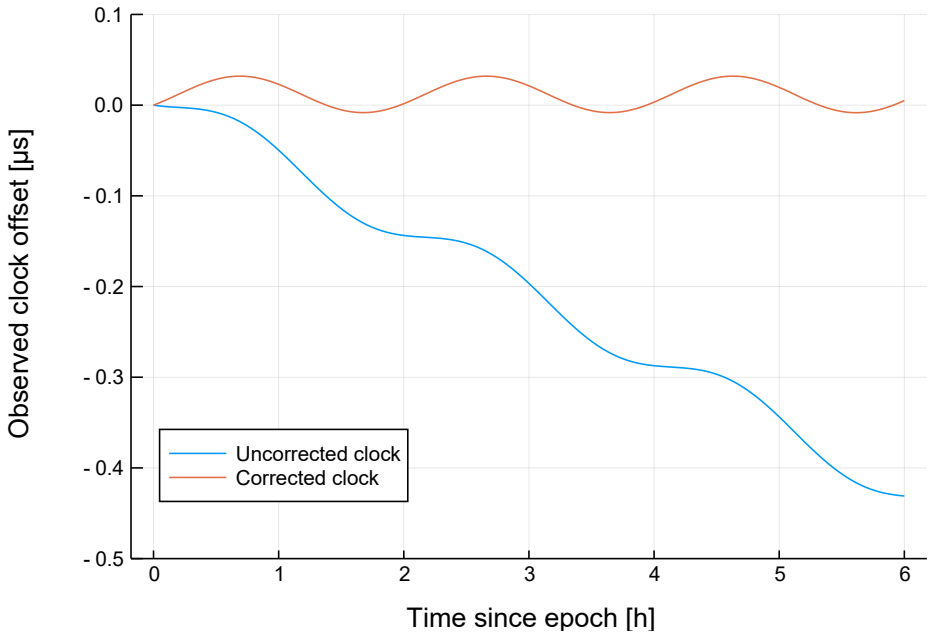

Figure 3.1: Observed clock offset of a satellite in a 100 km Lunar orbit, before and after correcting the secular effect by adapting the satellite clock frequency.

constant for this clock as well. Therefore, this effect can be corrected such that the gravitational time dillation of the receiver clock does not cause a drift with respect to the navigation satellite clocks. However, the velocity of this receiver, when considered in an ECI frame, consists of two terms; the velocity of the Moon in its orbit, and the velocity of the spacecraft around the Moon. The former of these is indeed roughly constant due to the almost circular velocity of the Moon. When a circular Lunar orbit is assumed, this second is constant as well. However, the vector sum of these velocities is effected by their motion, and as a result, the velocity magnitude of the satellite in an ECI frame changes with time. Therefore, a correction can be made for the nominal satellite velocity, but the cyclic effect will remain.
For such a satellite in low Lunar orbit, Figure 3.1 shows the observed clock offset for both the case with and without correcting the nominal effect. It should be noted that a clock offset of 0.1 µs corresponds to an effect of approximately 30 m on the pseudo range and thus can lead to considerable errors. After correction, the variation of the remaining effect is approximately 0.04 µs, resulting in a variation of approximately 12 m on the observations. This fluctuation is mainly a result of the eccentricity of the orbit of the Moon, which results in a variation of velocity of the Moon.
The time dilation factor is found through Equation 3.1, as per Botermann et al. [2014].

$$\gamma = \frac{1}{\sqrt{1 - \frac{v^2}{c^2}}} \tag{3.1}$$

3.3.1. Clock integration

As the relativistic dilation effects have an influence on the frequency of a clock with respect to another clock, an integration of this frequency is needed to determine the time indicated by these clocks. Due to the combined velocity of a satellite in Lunar orbit, an analytical expression for the receiver clock time becomes rather complex, hence is has been determined numerically.
A Runge-Kutta method of order 4 has been used to integrate the receiver clock. It is used to solve an initial value problem given by $\frac{dy}{dt} = g(y,t)$, and a known t_0 and y_0. Equation 3.2 and Equation 3.3 show the propagation from step i to $i+1$. Here, y_i is the solution, t_i is the time at step i, h is the size of the time step. k_1 through k_4 are given in Equation 3.4.

$$\vec{y}_{i+1} = \vec{y}_i + \frac{1}{6}(k_1 + 2k_2 + 2k_3 + k_4) \tag{3.2}$$

$$t_{i+1} = t_i + h \tag{3.3}$$

$$
\begin{aligned}
k_1 &= h \cdot g\left(y_i, t_i\right) \\
k_2 &= h \cdot g\left(y_i + \frac{k_1}{2}, t_i + \frac{h}{2}\right) \\
k_3 &= h \cdot g\left(y_i + \frac{k_2}{2}, t_i + \frac{h}{2}\right) \\
k_4 &= h \cdot g\left(y_i + k_3, t_i + h\right)
\end{aligned}
\tag{3.4}
$$

This method is used to solve Equation 3.5 to solve for the local true time, t_{local}. In this equation, t_{ref} is the reference time. In order to solve the clock time, t_{clock}, an extra term is added to represent the clock propagation rate f_c, as seen in Equation 3.6. By deviating this term from 1, the clock error can be corrected for a nominal velocity term. When correcting for a nominal velocity v_n, f_c should be multiplied with $\frac{1}{\sqrt{1-(v_n^2/c^2))}}$. For a 100 km lunar orbit, a nominal velocity of $v_n = 1924\,\mathrm{m\,s^{-1}}$ has been used, resulting in $f_c = 1 + 2.06 \times 10^{-11}$. This nominal velocity is equivalent to the RSS of the mean velocity of the Moon around Earth, and the velocity of the of the satellite around the Moon.

$$
\frac{dt_{local}}{dt_{ref}} = \sqrt{1 - \frac{v^2}{c^2}} \tag{3.5}
$$

$$
\frac{dt_{clock}}{dt_{ref}} = \sqrt{1 - \frac{v^2}{c^2}} \cdot f_c \tag{3.6}
$$

Integration of the receiver clocks is performed with steps of 2 s. This time step is taken as it will results in having many clock integration steps per ranging observation. This ensures that there are always two clock integration steps near the observation epoch, one before and one after, between which the interpolation of observation time can be performed.

3.3.2. Verification of velocity clock dilation

In order to verify the integration of the velocity clock dilation effect, and its correction, the effect is calculated for a GPS satellite. The GPS orbit used for this can be found in Table 3.1. This satellite has a constant velocity of $3873.96\,\mathrm{m\,s^{-1}}$, which gives a clock correction factor of $f_c = 1 + 8.349 \times 10^{-11}$. For this satellite, the clock integration is performed for a 24-hour time span using both the corrected and uncorrected clock. At the last epoch, which is at 86 400 s, the uncorrected clock indicates 86 399.999 992 794 74 s. Therefore, the moving clock on the satellite is 7.205 µs behind the static reference. The corrected clock indicates 86 400 s, and the difference between the clock time and epoch time is given at 0.0 µs, and thus the error after correction is below the numerical accuracy represented by the simulation.

Table 3.1: GPS orbit used for verification of the velocity clock dilation effect.

Kepler element	a	e	i	Ω	ω	θ	Central Body
Value	26 559.8 km	0	55°	272.85°	0°	11.68°	Earth

According to Fliegel and DiEsposti [1996], the GPS satellite clock is offset by a rate of −38 µs per day. Of this, −45 µs per day is to compensate the gravitational potential difference, and 7 µs per day is to compensate the velocity time dilation. This is in agreement with the 7.205 µs lag found after one day for the uncorrected GPS clock.

3.4. Determination of measurement times

When considering a set observation interval for an instrument, the exact moment of the observation is determined by the clock of the instrument. Hence, the timing of the LuNNaC observations is based on the receiver clock, causing receiver clock errors to influence the exact moment an observation is performed.
Therefore, after propagating from reference time t_i to t_{i+1}, it is checked whether the subsequent observation epoch is between t_i^c and t_{i+1}^c. When this is the case, the reference time t^{ref} should be found where t^c, the receiver clock time, equals the desired observation time. Initially, an estimate for this t^{ref} is made using linear interpolation. At this reference time, the clock time is then evaluated by performing the Runge-Kutta order

4 propagation from t_i to t^{ref}. The offset between observation time and interpolated clock time determines the convergence of the solution. Generally, this offset is below the threshold for a single bit in the 64 bits representation of these numbers. Hence, no further convergence is possible.

3.5. Reference orbits

The lunar navigation system is mainly designed with orbit determination of satellites in orbit around the moon in mind. Therefore, when simulating a case for received navigation signals and obtained navigation solution from those, a receiver in Lunar orbit is most representative. The reference orbits used to perform case studies are presented here. Table 3.2 presents the orbits used for a selection of Lunar missions, which has been used for the selection of orbits.

Table 3.2: A selection of Lunar satellites, and their orbits based on eoPortal. The orbits are shown as apoapsis x periapsis altitude.

Mission	Launch year	Initial orbit	Optional secondary orbit
Clementine	1994	4594x2162 km polar	400x1225 km polar
SMART-1	2003	2200x4600 km polar	
Chang'e-1	2007	200x200 km	
SELENE	2007	100x100 km polar	
Chandrayaan 1	2008	100x100 km polar	
LRO	2009	50x50 km polar	
Chang'e-2	2010	100x100 km	100x15 km
Grail	2011	55x55 km polar	
Chang'e-3	2013	100x100 km	100x15 km
LADEE	2013	50x50 km retrograde equatorial	

3.5.1. Low Lunar orbit

Firstly, a Low Lunar orbit is used as the receiver orbit. As observed from the selected missions, a 100x100 km orbit is quite a common choice for Lunar satellites and as intermediate orbit for landers. Even though polar orbits are quite common as well, the simulations will be performed using an equatorial orbit to ensure that the satellite passes the Lunar far side, independent of the phase of the Moon in its orbit. Low altitudes for Lunar satellites are quite common because of the high ground resolution that can be obtained. Although the Moon has no atmosphere, which removes the drag effect that occurs for satellites in low Earth orbits, Lunar orbits at very low altitudes can, however, become quite unstable because of the irregular gravity field. Table 3.3 indicates the Kepler elements for this Low Lunar reference orbit.

Table 3.3: Orbital elements for the Low Lunar orbit used as reference orbit.

Kepler element	a	e	i	Ω	ω	θ	Central Body
Value	1838.1 km	0	0°	0°	0°	0°	Moon

3.5.2. Lunar transfer orbit

A secondary reference orbit is needed to test the Lunar navigation system for such a case. The most relevant low-energy transfer use-case is considered to be a Hohmann transfer. The used Kepler elements at the start of the transfer are as seen in Table 3.4.

Table 3.4: Orbital elements for the Hohmann transfer orbit used as reference orbit.

Kepler element	a	e	i	Ω	ω	θ	Central Body
Value	198478.2 km	0.96694	5.16°	125.08°	28.775°	0°	Earth

4

Ranging observations

The LuNNaC satellites will continuously transmit their navigation messages. For the purpose of this research, the carrier frequency is assumed to be centered around the same frequency as the GPS L1 band, or the Galileo E1 band at 1575.42 MHz. Two observations will be considered on this band; the code pseudorange measurement and the carrier phase measurement, both of which are discussed in the following section. This is followed by a discussion on the path of the signals, and when a signal is blocked and/or disturbed. Here, the effect of neglecting signals that pass through the ionosphere is considered. As LuNNaC signals have to travel further to the Moon than regular GNSS signals to earth, the former lose more power during this path. As a result, the noise on the measurements will be larger. The link budget of the signals, as well as its effect on the measurement error is explained.

4.1. Obervation types

The LuNNaC receivers are assumed to be able to perform observations on both code and carrier phase of the navigation signal. The navigation code is a repeating pseudo random signal which is modulated on top of the navigation signal by the transmitter. This allows a receiver to generate the same pseudo random signal and correlate it with the received signal. By determining how much the signal must be shifted in time to achieve a high level of correlation, the travel time of the signal, and thus the pseudorange, can be obtained. Due to the length of the chips of the code, the achievable accuracy of this pseudorange is relatively coarse.
On the contrary, carrier phase observations are obtained by comparing the carrier of the received signal with a generated reference signal. By tracking the passage of relative phase between the signals, changes in relative distance between transmitter and receiver can be observed. Due to the high frequency of the carrier phase, the wavelength of the carrier is much shorter than the chips of a navigation code. Therefore, carrier phase observations can be of much higher precision than pseudorange observations. However, whereas the code signal is sufficiently long before repetition to be able to completely resolve the pseudorange, the different periods of the carrier phase cannot be distinguished, and thus it can not be used as an absolute measure of distance.
For both creating a navigation algorithm using those observations, and for simulating the observations, observation equations are needed. These are further deduced for both types of observations in this section.

4.1.1. Pseudorange observation

The pseudorange is directly obtained from the measure of travel time of a signal from transmitter to receiver. This observed travel time, $t_r^s(t)$, can be written as in Equation 4.1, where t is the epoch time, $t_r(t)$ the receiver clock time, t^s the transmitter clock time, and $\tau_r^s(t)$ the true signal travel time:

$$t_r^s(t) = t_r(t) - t^s(t - \tau_r^s(t)) \tag{4.1}$$

As the travel distance and travel time of the signal are linked through the speed of light, the pseudorange can be written as Equation 4.2. In this equation, P_r^s is the pseudorange, c is the speed of light, and ϵ_{rP}^s represents any other remaining error, such as due to atmospheric delays or measurement noise.

$$P_r^s(t) = c \cdot (t_r(t) - t^s(t - \tau_r^s(t))) + \epsilon_{rP}^s(t) \tag{4.2}$$

At any given time, the clocks can be assumed to be a linear combination of epoch time and time-dependent clock error; $t_r(t) = t + \delta t_r(t)$ and $t^s(t) = t + \delta t^s(t)$ for the receiver and transmitter clock respectively. Substituting those into Equation 4.1 or Equation 4.2 allows nominal time, errors and travel time to be separated in the equation. This is important for two reasons: Firstly, during the parameter estimation process, the receiver clock error is an estimated parameter, while an estimate for the transmitter clock error is broadcasted. Having travel time and clock error separated simplifies the derivatives with respect to estimators, consisting of 3 position coordinates and receiver clock errors. Moreover, both $t_r(t)$ and $t^s(t)$ have the linear t dependency, which means that the numerical accuracy of these numbers within the simulation decreases with epoch time due to a fixed size floating point representation. When keeping the signal travel time, and thus geometric range, within $t^s(t - \tau_r^s(t))$ will limit the accuracy of this term, and hence the accuracy decreases with increasing epoch times. Since the geometric range term is the dominant term in the pseudorange observations, this will result in a large, and unnecessary error when simulating the signals.
Substituting clock times for true times with clock errors in Equation 4.2, one can rewrite $t^s(t - \tau_r^s(t))$ as $t - \tau_r^s(t) + \delta t^s(t - \tau_r^s(t))$. Since $c \cdot \tau_r^s(t)$ is the geometric range between transmitter at transmission time, and receiver at reception time, rewriting Equation 4.2 in this form allows us to write the pseudorange in terms of geometric range, as seen in Equation 4.3. As a result, the main term of the pseudorange measurement, which is the geometric range, can use the full numerical accuracy of its type, and the simulation accuracy is not limited by terms which grow in time.

$$P_r^s(t) = \rho_r^s(t) + c\left(\delta t_r(t) - \delta t^s\left(t - \tau_r^s(t)\right)\right) + \epsilon_{rP}^s(t) \tag{4.3}$$

The term $\delta t^s\left(t - \tau_r^s(t)\right)$ represents the transmitter clock error at transmission time. It is assumed that transmitters contain high stability (atomic) clocks, and corrections are broadcasted, allowing this error to be largely recovered, and therefore have a negligibly small effect with respect to other errors. Therefore, it has been decided to not include this effect in both simulation and navigation, such that $\delta t^s(t) = 0$ is used.

4.1.2. Carrier phase observations

Besides correlating navigation codes, the phase of the carrier wave can be tracked by a receiver. As the wavelength of the carrier is much shorter than a single chip length, these observations can achieve a much lower noise level. The observation, in essence, consists of a difference between receiver reference and transmitted carrier phase, $\phi_r - \phi^s$, and an integer number of cycles, N_r^s, as can be seen in Equation 4.4. Here, τ is the travel time of the signal. This last terms originates from the rapidly repeating pattern of carrier phases, which makes it that the received phase can be measured, but not the exact cycle. While fix to a satellite is maintained, integration of the difference between received carrier and reference signals leads to correctly tracking the change in number of cycles. Hence, N_r^s remains constant for a single satellite while no loss of lock occurs.

$$\phi_r^s(t) = \phi_r(t) - \phi^s(t - \tau_r^s(t)) + N_r^s \tag{4.4}$$

The transmitted and reference phases can be expressed as Equation 4.5. Three terms can be identified in this equation. It contains a term for the phase at a reference time (t_0), one for the current phase relative to that at the reference time, and finally a corrective term for transmitter and receiver clock errors. This same equation is valid for both reference and transmitted phases.

$$\phi(t) = \phi(t_0) + f(t - t_0) + f(\delta t(t) - \delta t(t_0)) \tag{4.5}$$

One option for simulating the navigation observations is to calculate both reference phase and transmitted phase, and calculate $\phi_r^s(t)$ from that. However, the linear dependency on t causes the magnitude of these numbers to grow rapidly in time. With limited numerical precision, this means that the numerical accuracy of ϕ_r and ϕ^s decreases with time, which is undesirable. The phase difference, however eliminates the $f \cdot t$ term, as seen in Equation 4.6.

$$\phi_r^s(t) = f\tau_r^s + \phi_r(t_0) - \phi^s(t_0) + f(\delta t_r(t) - \delta t_r(t_0) - \delta t^s(t - \tau_r^s(t)) + \delta t^s(t_0)) + N_r^s \tag{4.6}$$

Multiplying this by the wavelength, λ, results in the phase observation equation in meters, as seen in Equation 4.7. Furthermore, in this equation a bias term, A_r^s, is introduced. This term remains constant for the duration of a lock on a satellite. It is further defined in Equation 4.8. Finally, the remaining measurement errors are denoted by ϵ_{rL}^s. For this research, this term is limited to measurement errors.

$$\lambda \cdot \phi(t) = \rho_r^s(t) + c\left(\delta t_r(t) - \delta t^s\left(t - \tau_r^s(t)\right)\right) + A_r^s + \epsilon_{rL}^s \tag{4.7}$$

$$A_r^s = \lambda N_r^s + \lambda\left(\phi_r(t_0) - \phi^s(t_0)\right) + c\left(\delta t_r(t0) - \delta t^s(t_0)\right) \tag{4.8}$$

4.2. signal travel path effects

The path a radio signal travels can have some effect on the observations. Firstly, it should be noted that due to the finite speed of light, the transmitter can move some distance between the transmission and reception time. Therefore it can not be assumed that the signal originates from the location of the transmitter at reception time. This phenomenon is called the light time effect, for which an iterative method will be given to determine the transmission location and travel time.
Furthermore, large solid objects can completely block the signal and prevent its reception. On Earth, this is very noticeable in mountainous or urban areas, where signal blockage might occur. In space, the major cause for a blocked signal is eclipse by a heavenly body; the Earth and Moon for this specific case. The conditions and assumptions are discussed for which such blockage occurs. For the purpose of this research, multipath effects are neglected. These are most likely to occur due to the shape of the antenna, and how it is positioned on the vehicle, rather than based on external conditions, and therefore can not be determined in this initial research.
Finally, atmosphere and ionosphere can delay a radio signal. The magnitude of this delay is dependent on the wavelength of the signal. Therefore, the use of dual frequency GNSS receivers allow one to correct for these effects. With Lunar navigation using LuNNaC, signals only need to travel through atmosphere and ionosphere while a transmitter is almost behind the Earth with respect to the Moon. As a result, only a small part of the measurements will be affected by ionospheric delay. In order to investigate the need of the application of dual frequency transmitters and receivers, the magnitude of completely neglecting such observations is investigated.

4.2.1. Light-time effect

Any radio signal traveling through a vacuum travels with the finite speed of light. As a result, a transmitter in Earth orbit has moved in the time between the transmission and reception of a signal, and it can not be assumed that the signal originated from the location of the transmitter at reception time. For the Earth-Moon distance, this travel time is about 1.3 s. Considering the transmitters have a velocity of several kilometers per second, the transmitter displacement in this time is in the order of magnitude of several kilometers.
The geometric range a signal travels can thus be described by Equation 4.9, where ρ is the geometric range traveled by the signal, t is the time of reception, τ is the travel time of the signal $\vec{r}_u(t)$ is the time dependent position vector of the receiver, and $\vec{r}^s(t)$ is the time dependent position vector of the transmitter.

$$\rho = |\vec{r}_u(t) - \vec{r}^s(t - \tau)| \tag{4.9}$$

Furthermore, the travel time of the signal, assuming it is in a perfect vacuum, is given by Equation 4.10, where c is the speed of light.

$$\tau = \frac{\rho}{c} \tag{4.10}$$

As Equation 4.10 and Equation 4.9 are dependent on one another, while the position vectors are solved for numerically, no direct solution for the range exists. However, one can make use of an iterative solution, called the Newtonian method, as notated by Equation 4.11, where ρ_i is the signal travel distance after the ith iteration. As the travel distance for the first iteration, $\rho_0 = 0\,\text{m}$ is used.

$$\rho_{i+1} = |\vec{r}_u(t) - \vec{r}^s(t - \frac{\rho_i}{c})| \tag{4.11}$$

4.2.2. Signal blockage

Whenever a transmitter and receiver are positioned such that a large body, such as Earth or the Moon, is directly in the line of sight path, no signal will be received. To check whether the line of sight is blocked by a given body, two steps are taken.

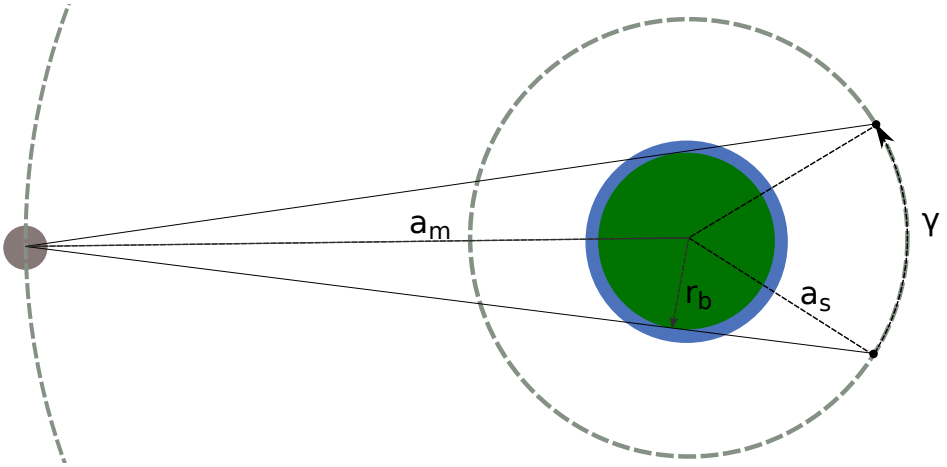

Figure 4.1: Eclipse angle for a navigation satellite in an Earth centered reference frame co-rotating with the Moon.

Firstly, the transmitter and receiver must both be on another side of the body for blockage to occur. This is only the case when the distance between transmitter and receiver is larger than distance between the horizon of the body and both the transmitter and receiver, which can be checked through Equation 4.12. Here, $\vec{r}$ are location vectors, where the subscripts s, r, and b stand respectively for transmitter, receiver and body. The body radius is indicated by R_b. The maximum body radius is used for this, in order to make the most conservative estimate for the blockage when compared to using the mean body radius.

$$\sqrt{\max(\{|\vec{r}_s - \vec{r}_b|, |\vec{r}_r - \vec{r}_b|\})^2 - R_b^2} < |\vec{r}_r - \vec{r}_s| \tag{4.12}$$

The second condition for signal blockage to occur is for the transmitter and receiver to be sufficiently aligned with the body that the surface of the body extends through the signal line. Equation 4.13 checks whether the line passing through transmitter and receiver comes within the radius of the body.

$$|\vec{r}_r - \vec{r}_b - ((\vec{r}_r - \vec{r}_b) \cdot (\frac{\vec{r}_b - \vec{r}_r}{|\vec{r}_b - \vec{r}_r|}))(\frac{\vec{r}_b - \vec{r}_r}{|\vec{r}_b - \vec{r}_r|})| < R_b \tag{4.13}$$

When both of these expressions are true, the signal is blocked by the considered body. In the case of the LuNNaC navigation signals, blockage of the signal by both Earth and Moon must be considered.

4.2.3. Ionospheric measurements

In certain cases, before and after the navigation signal transmitted by a satellite is blocked by Earth, the navigation signal travels through the ionosphere. The free electrons in this region cause a change in the observed speed of the signal through refraction and diffraction. As a result, an error will be induced on the phase and code observations.

Three straightforward approaches to dealing with this error source are identified. Firstly, the ionospheric delay can be modeled in order to compensate the observations. This approach, however, tends to be rather inaccurate, and can be rather computationally expensive. Secondly, as the ionospheric delay is dependent on the carrier frequency of the signal, ionospheric free combinations of observations can be made when the navigation signal is transmitted on at least two different frequencies by the navigation satellite. For simplicity of both transmitter and receiver, however, it would be desirable to limit the system to transmission of a single frequency. Finally, one can choose to completely disregard observations that pass below a specified threshold altitude above Earth. Especially since such observations that contain ionospheric delays are rather scarce, this is considered to be the most appropriate approach for the LuNNaC system. The altitude used for this threshold is set at 800 km and is incorporated in the model as an increase in maximum Earth radius as used in the signal blockage, as seen in subsection 4.2.2, identical to Sun et al. [2013]. Ionospheric errors are not induced on signals that travel above this threshold.

Using an analytic approach, a first estimation can be made of the length of eclipses, as well as on the effect of neglecting the ionospheric observations on the length of this eclipse. For this, an observer near the moon is

simplified as a circular Earth orbit with the same semi-major axis as the orbit of the Moon. When considering a co-rotating system with the observer, as shown in Figure 4.1. The Earth centered eclipse angle, γ, show in this figure can be calculated using Equation 4.14

$$\gamma = 2\arcsin\frac{r_b}{a_s} + 2\arcsin\frac{r_b}{a_m} \tag{4.14}$$

In this equation r_b represents the radius of the spheroid blocking navigation signals. Furthermore, a_s and a_m represent the semi-major axes of the circular orbits for respectively the transmitter and the Moon. In this system, the transmitter has a mean motion of $n_s - n_m$, where n_s and n_m are the mean motions of a transmitter and the moon in a non-rotating system. Therefore, the eclipse time, t_e, is as indicated by Equation 4.15.

$$t_e = \frac{\gamma}{n_s - n_m} \tag{4.15}$$

From this, the eclipse time from blockage by Earth only, assuming a maximum radius of $r_E = 6378.1$ km is 2587 s. In comparison, when the observations traveling below 800 km are disregarded, the eclipse times increases to 2943 s. Meanwhile, the orbital period of a 14 000 km orbit is 16 486 s. Hence, the eclipse time rises from 15.7% to 17.9% of the orbital period. When three satellites are equally spaced in this orbit, the fraction of orbital period in which all three satellites in this co-rotating plane are in view decreases from 52.9%, to 46.4%.

4.2.4. Signal obstruction verification

The numerical method used to determine if the navigation signal is blocked by body, shown in subsection 4.2.2, is verified by comparing it to the analytical calculation of the eclipse time for blockage by the Earth, from subsection 4.2.3. In order to make a proper comparison between the numerical and analytical case, the numerical simulation must be performed with two circular orbits in the same plane. Firstly, as the receiver, the orbit of the Moon is taken where the eccentricity of the orbit is set to 0.0 to make it circular. The orbit for the transmitter is taken to be the same as this circular receiver orbit, except the semi-major axis, which is changed to 14 000 km to represent the proper PECMEO orbit. Because of the identical inclination, right ascension of the ascending node, and true anomaly, the receiver, transmitter and Earth will be on a single line at the start epoch, where receiver and transmitter are at the same side of the Earth. Therefore, no blockage occurs at the start of the simulation, and the full eclipse is captured within a single orbit of the transmitter satellite.

For the numerical calculation of eclipse time, time steps of 0.01 s are taken. At each epoch, the position of the transmitter and receiver is calculated, and it is determined if an instantaneous signal would be blocked by the Earth. From this, it is found that there is 2943.45 s between the first and last epoch where blockage occurs. Because of the time resolution of the simulation, the eclipse time must be between 2943.45 s and 2943.47 s.

Calculating the eclipse using the analytical method using Equation 4.14 and Equation 4.15, results in an eclipse time of 2943.4673 s. Therefore, the numerically calculated eclipse time is in agreement with the direct calculation of the eclipse time. Hence, it can be concluded that the conditions for signal blockage are correct and properly implemented.

4.3. Measurement Noise

For GPS, the signal received on Earth has a SNR well below 1, and as a consequence the signal is completely burried in noise. Correlation with the correct PRN signal, however, causes despreading of the signal to the bandwidth of the navigation data, and therefore results in a large SNR increase.

The *carrier-to-noise density*, denoted as C/N_0, determines the accuracy with which the code pseudorange and carrier phase measurements are performed. The first step to determining these errors, is by finding C/N_0 for a given pair of satellites from their link budget. Afterwards, from a direct relationship between the variance and C/N_0, the variance is determined, allowing the errors to be estimated from a normal distribution.

4.3.1. Link budget

The link budget for the navigation signal in this research is considered in three steps. Firstly, the power level of the transmitted navigation signal, as received by the receiver, is determined. Afterwards, the noise level at the output of the receiver is determined. Finally, these numbers are combined into the precorrelation SNR and C/N_0.

The signal transmitted by the navigation satellites loses power density with distance from the transmitter. This free space loss is given by Braasch and van Dierendonck [1999] as Equation 4.16.

$$L_0 = \left(\frac{\lambda}{4\pi R}\right)^2 \tag{4.16}$$

In this equation, L_0 is the free space loss, defined as the ratio between received and transmitted signal power; $L_0 = \frac{P_S}{P_T}$ when P_S is the signal power at the receiver while P_T is the signal power transmitted. Moreover, λ is the signal wavelength, and R is the distance between transmitter and receiver. Considering the LuNNaC signal on L1 GPS frequency, at 1575.42 MHz, which corresponds to a wavelength of 0.1903 m, and a nominal distance being equal to the lunar semi-major axis of 384.40×10^3 km, as per Lissauer and de Pater [2013] and Standish [2001], a nominal free-space loss of -208 dB is obtained. This is a considerable stronger attenuation compared to GPS, where the free-space loss is approximately -182 dB according to Fisher and Ghassemi [1999].

The noise power in the signal bandwidth B can be approximated by Equation 4.17.

$$P_N = kT_E B \tag{4.17}$$

Here, k is Boltzmann's constant, and T_E is the effective noise temperature in Kelvin, resulting in P_N, the noise power, in W. When pointing the receiving antenna towards the constellation of navigation satellites, the Earth is in view of the antenna as well. Therefore, T_E is taken to be 290 K, in accordance with Fortescue et al. [2011] and Moreau et al. [2000].

Braasch and van Dierendonck [1999] consider 513 K to be a typical effective noise temperature for GPS receivers. This work, however, does not particularly consider space-based GPS receivers. Chen et al. [2019], on the other hand, consider their system noise temperature for their Lunar cubesats at 135 K.

From the obtained signal power and noise levels, the precorrelation SNR can be obtained as a straight ratio using Equation 4.18, where P_S is the received signal power.

$$SNR = \frac{P_S}{P_N} \tag{4.18}$$

From this, the carrier-to-noise density bandwidth is obtained in Hz using Equation 4.19. The corresponding value in dB Hz is obtained by converting the value to a logarithmic scale.

$$C/N_0 = SNR \cdot B \tag{4.19}$$

It should be noted that both C/N_0 and the noise power are linearly proportional to the post-filtering bandwidth. As C/N_0 is inversely proportional to noise power, the bandwidth is completely eliminated from this link budget. Hence, substituting Equation 4.17-4.18 into Equation 4.19 yields a simplified expression for C/N_0, as seen in Equation 4.20. In this equation, P_T is the transmitted signal power.

$$C/N_0 = \frac{P_T L_0}{kT_E} \tag{4.20}$$

When considering the nominal link budget for LuNNac, with a signal power of 119 W, and a transmitter antenna gain of 16.5 dB, as discussed in subsection 2.2.2, a value for C/N_0 of 33.1 dB Hz is obtained. For the nominal link budget, the Moon semi-major axis is assumed as distance between Earth and the receiver, and the transmitter is assumed to be in the midway point between closest to and furthest away from the moon, which yields a nominal distance of 384.7×10^3 km. The C/N_0 values for the entire intended operating space are indicated in Figure 4.2. It can be seen that, while GPS generally operated at a C/N_0 above 35 dB Hz, the LuNNaC system will generally operate slightly below this point. Although the signal travel distance is greatly increased, more directional antennas can be used, resulting an a larger effective isotropic transmitted power.

4.3.2. Relation between error and signal strength

Measurement noise on the navigation signals is normally distributed. The expectation for the magnitude of the noise is zero, or $\mathbb{E}(\epsilon^s_{r\,P}) = 0$ and $\mathbb{E}(\epsilon^s_{r\,L}) = 0$, thus the measurement noise has a zero mean. Furthermore, as discussed, the variance of the observation error, both for code and carrier-phase measurements, is dependent on the carrier-to-noise density. The relations shown are obtained from Braasch and van Dierendonck [1999].

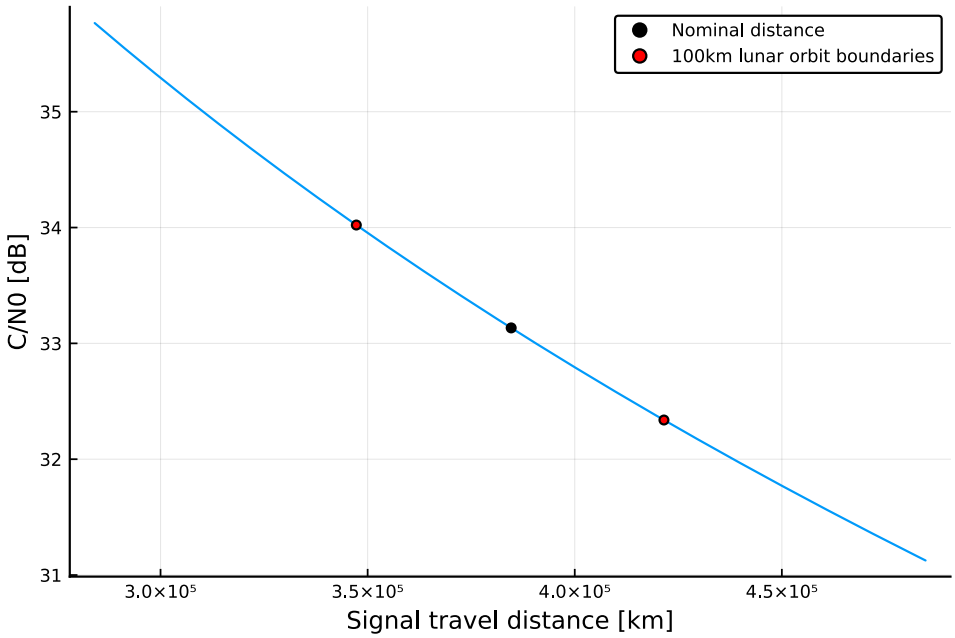

Figure 4.2: Carrier-to-noise density for the LuNNaC signals within the designed operating distances. The extreme distances for a 100km circular Lunar orbit have been indicated.

Firstly, the thermal noise for the tracking error of the pseudorange measurements is as estimated by Equation 4.21.

$$\sigma_\tau^2 \approx \frac{B_{Lc}\, d}{2C/N_0}\left[1 + \frac{1}{T \cdot C/N_0}\right] \tag{4.21}$$

In this equation, σ_τ^2 is the tracking error variance in fraction of PRN chips squared. Furthermore, $B_{L,c}$ is the code tracking loop bandwidth in Hz, d the dimensionless early-to-late correlator spacing, and C/N_0 the signal carrier-to-noise density in ratio-Hz. Applying this to the nominal C/N_0 yields a nominal standard deviation for the pseudorange noise of 6.5 m. Applying this equation to the described link budget for the operation range of the LuNNaC signals yields Figure 4.3, where the pseudorange standard deviation is shown in relation to the distance between transmitter and receiver. The shown values are limited to a 65×10^3 km sphere around the moon.
Moreover, for the carrier phase measurements, the tracking error variance is estimated by Equation 4.22.

$$\sigma_\theta^2 = \frac{B_{Lp}}{C/N_0}\left[1 + \frac{1}{(2T)C/N_0}\right] \tag{4.22}$$

Here, σ_θ^2 is the carrier phase tracking error variance in rad^2, B_{Lp} the carrier phase tracking loop bandwidth in Hz, T the predetection integration interval in s, and C/N_0 the carrier-to-noise density, again in ratio-Hz. For B_{Lp}, a value of 5 Hz is used, and 20 ms is used for T , in accordance with Braasch and van Dierendonck [1999]. For the nominal link distance, the standard deviation of the carrier phase observation error is 1.5 mm. Figure 4.4 shows the variation of this standard deviation within the design space around the moon.

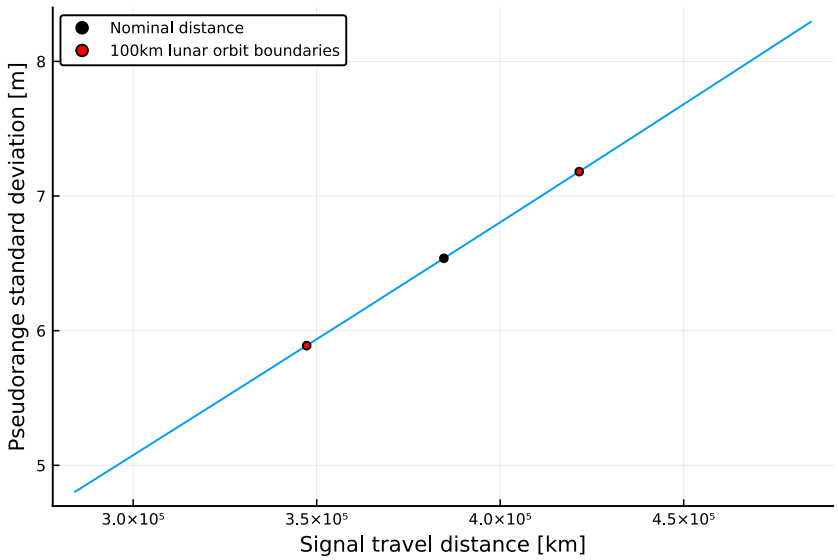

Figure 4.3: Variation of the standard deviation of pseudorange observations within the Moon hill sphere, within which a receiver is assumed to be. The nominal value, and extreme values for a 100 km circular Lunar orbit are indicated.

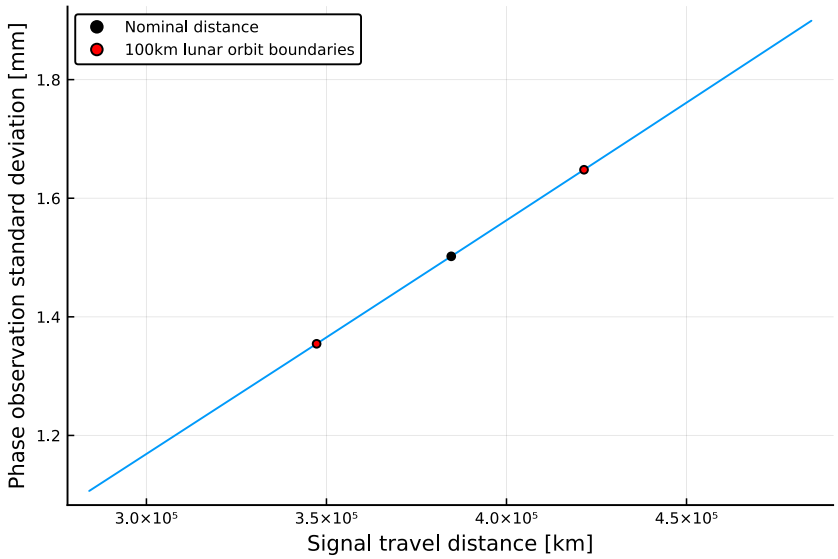

Figure 4.4: Variation of the standard deviation of carrier phase observations within the Moon hill sphere, within which a receiver is assumed to be. The nominal value, and extreme values for a 100 km circular Lunar orbit are indicated.

5

Navigation constellation design and optimization

The design of the navigation constellation is performed through optimization of the geometry. This chapter will start with defining the geometric performance of a navigation constellation. Furthermore, the optimization process is discussed, and the the resulting design is presented.

5.1. Geometric navigation performance

The geometry of the navigation constellation has a large influence on the quality of the final solutions. The accuracy of various estimated parameters can be estimated through the dilution of precision (DOP). Most importantly, the GDOP (geometric dillution of precision) predicts the combined navigation accuracy through Equation 5.1. Here, the 1σ navigation accuracy is predicted, when $UERE$, or User Equivalent Range Error, is the RSS of the 1σ value for error along the direction of the observation.

$$1\sigma \text{ Navigation Accuracy} = UERE \times GDOP \tag{5.1}$$

5.1.1. Dillution of precission

GDOP can be found through Equation 5.2, where G_{xx}, G_{yy}, G_{zz} and G_{bb} are the diagonals of G, which is found through $G = (H^T H)^{-1}$. Here, H is a matrix consisting of a 4-dimensional vectors for each transmitter with a clear line of sight to the receiver. These 4-dimensional vectors consist of the line of sight vector, e, a unit 3-dimensional unit vector pointing from the corresponding transmitter to the receiver, and a value of 1 for the receiver clock error parameter. This same matrix H is used for solving a point position solution, and is further elaborated in section 6.2.

$$GDOP = \sqrt{G_{xx} + G_{yy} + G_{zz} + G_{bb}} \tag{5.2}$$

Hence, geometric performance of a navigation system can be studied without knowledge of error sources, nor solving the entire navigation solution. Through comparison of GDOP, one constellation can be objectively compared to another, allowing an optimization to be performed.

5.2. Constellation design

From the direct impact of the GDOP on navigation accuracy, it can be concluded that the position of navigation satellites will have a large impact on navigation accuracy. Therefore, before any navigation performance can be determined, the orbits of the navigation satellites need to be known. Moreover, although the purpose of this thesis is not to find the best possible constellation, a near-optimal constellation needs to be used for the assessment of system performance, as using a less-than optimal constellation will influence the navigation performance adversely, and therefore influences suggestions on further development.

Hence, an optimization of the satellite orbits within the constellation has been performed. A limited design space, using various constraints, as well as optimizing on navigation geometry rather than complete

navigation accuracy reduce the complexity of this optimization. The former is discussed in the following section, after which the latter is discussed. Finally, the optimization results are discussed and the obtained constellation is presented.

5.2.1. Design space

In order to greatly simplify the process of constellation design, various assumptions will be made on the orbits of the navigation constellation. Firstly, as the constellation design is based on PECMEO orbits, the satellites are assumed to only be placed in three orthogonal planes. Meanwhile, all satellites can be considered to be in circular orbits, all with equal orbital radius and equidistant spacing within the plane.
For the orbits of the PECMEO satellites, a constant orbital radius of 14 000 km is assumed. This places the satellites well below various GNSS transmitters, ensuring a good coverage of these signals. Meanwhile, increasing this altitude might decrease coverage, and therefore have a detrimental effect on ephemeris precision. In turn this will increase the EURE, reducing the quality of the navigation solution. On the other hand, increasing the orbital altitude will surely improve the GDOP for navigation with a Lunar receiver due to the increased spacing between the satellites. Hence, an optimization purely based on GDOP should have a fixed altitude, as the effect on ephemeris error in not considered.
The PECMEO satellites are assumed to be spaced along constant intervals on the orbits. The constellations consist of 3 satellites for each of the three orbits, resulting in a spacing of 120° between satellites in an orbit.
Four optimization parameters are considered; two rotation parameters, which dictate the orientation of the constellation, and two initial true anomaly parameters to specify the relative phasing of satellites between the planes. These parameters are represented by $\vec{x} = [\Delta i_1, \Delta i_2, \Delta\theta_2, \Delta\theta_3]^T$. Here, the indices specify the orbital plane to which these parameters are applied.
A third rotation axis is not considered. The first two rotation axes, to which Δi_1 and Δi_2 are applied, are chosen such that they are orthogonal to the angular momentum vector of the orbit of the Moon. Therefore, the effect of changing the orientation of the constellation around this third axis will be captured by the almost circular orbit of the Moon when simulating for a full orbital period of the Moon. Moreover, the movement of the navigation satellites around their orbit removes the need for a third initial true anomaly parameter. Since an orbit of the Moon has a much longer time period than the navigation satellite orbital period, the relative phasing of the first orbit is not considered as the movement of the Moon within a single orbit of PECMEO satellites is negligible.

The following procedure is used to combine these parameters into Kepler elements. The first orbital plane to be defined is, before modification with the optimization parameters, the plane that is orthogonal to that of the orbit of the Moon. The right ascension of the ascending node of this orbit is identical to that of the orbit of the Moon, defined by $\Omega_1 = \Omega_m$, which is not modified by the optimization parameters. The first rotation parameter is directly applied to the inclination of this orbit through $i_1 = i_m + \frac{\pi}{2} + \Delta i_1$, where the parameter is limited by $-\frac{\pi}{4} \leq \Delta i_1 \leq \frac{\pi}{4}$. These can be used to define $\vec{H}_1$ through Equation 5.3 and 5.4.

$$H = \sqrt{a \cdot \mu} \tag{5.3}$$

$$\vec{H} = H \cdot \begin{bmatrix} \sin i \sin \Omega \\ -\sin i \cos \Omega \\ \cos i \end{bmatrix} \tag{5.4}$$

For the second orbital plane, a non-rotated angular momentum vector, $\vec{H}_{2\prime}$ is defined first through Equation 5.4, where $\Omega_{2\prime} = \Omega_1 + \frac{\pi}{2}$, and $i_{2\prime} = \frac{\pi}{2}$. The rotation of this second plane due to the second optimization parameter Δi_2, is found through Rodrigues' rotation formula, as shown in Equation 5.5. Therefore, Δi_2 does influence the inclination of this plane, but in order to keep the three planes orthogonal, it can not directly be applied to the inclination parameter. In Equation 5.5, $\vec{H}_2$ is the angular momentum vector for the second orbital plane, $\hat{H}_1 = \frac{\vec{H}_1}{H}$ is the normalized $\vec{H}_1$ vector. This rotates $\vec{H}_{2\prime}$ with $\vec{H}_1$ as rotational axis, ensuring these vectors remain orthogonal. The parameter Δi_2 is bounded by $\frac{\pi}{4} \leq \Delta i_2 \leq \frac{\pi}{4}$.

$$\vec{H}_2 = \vec{H}_2' \cos \Delta i_2 + \left(\hat{H}_1 \times \vec{H}_2'\right) \sin \Delta i_2 + \hat{H}_1 \left(\hat{H}_1 \cdot \vec{H}_2'\right) (1 - \cos \Delta i_2) \tag{5.5}$$

Inclination and right ascension of the ascending node are recovered from the angular momentum vector through Equation 5.6 and 5.7 in order to obtain i_2 and Ω_2.

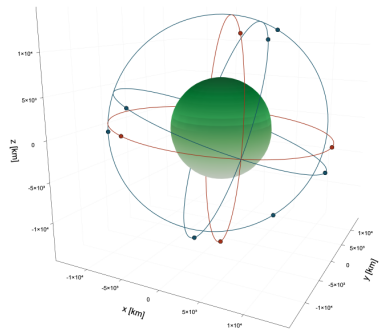

(a) $\Delta i_1 = 0°$ (red) to $\Delta i_1 = 15°$ (blue)

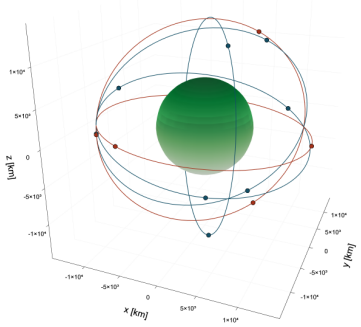

(b) $\Delta i_w = 0°$ (red) to $\Delta i_w = 15°$ (blue)

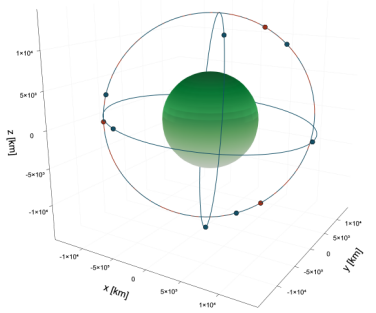

(c) $\Delta\theta_2 = 0°$ (red) to $\Delta\theta_2 = 15°$ (blue)

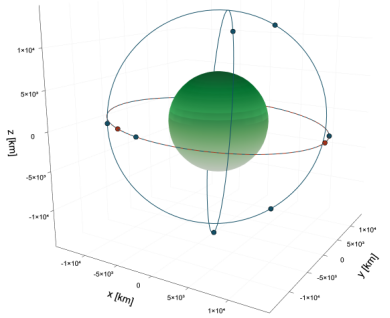

(d) $\Delta\theta_3 = 0°$ (red) to $\Delta\theta_3 = 15°$ (blue)

Figure 5.1: Visualization of the effect of each of the four optimization parameters. The constellation depicted in red is identical in each figure, and has the design vector $\vec{x} = [0°, 0°, 0, 0]^T$. The blue constellations have one parameter modified by 15°.

$$\cos i = \frac{H_z}{H} \tag{5.6}$$

$$\frac{\sin\Omega}{\cos\Omega} = \frac{H_X}{H_Y} \tag{5.7}$$

The final orbital plane is orthogonal to the first and the second, hence its angular momentum vector can be found through Equation 5.8. The inclination, i_3 and right ascension of the ascending node, Ω_3, are found through Equation 5.6 and 5.7.

$$\vec{H}_3 = H\left(\hat{\vec{H}}_1 \times \hat{\vec{H}}_2\right) \tag{5.8}$$

The effect each of the optimization parameters has on the constellation is shown in Figure 5.1.

5.2.2. Optimization objectives

The goal of the optimization is to find the optimum navigation geometry for the given constraints. Such an optimum geometry should have a low GDOP throughout is operational life. However, the position of the Moon in its orbit is of large influence on the navigation geometry of this problem. Therefore, the GDOP should not only be taken at a single time, but rather be analyzed throughout the orbit of the moon. This is done by sampling the GDOP for one orbital period of the Moon at intervals of 200 s.

In order to optimize the GDOP, the time-series that has been obtained must be represented by a small number of fitness functions. Firstly, it is desirable to have an overall low GDOP value, which has been represented by the mean of the GDOP values throughout the time series. Furthermore, whenever a navigation satellite moves behind the earth, with respect to the Moon, a sharp increase in GDOP is observed, which is amplified much further when a second satellite leaves the view. In order to improve these worst-case scenarios, the maximum

Table 5.1: The limits of the four optimization parameters used to define the navigation constellation.

Parameter	Min	Max
Δi_1 (x_1)	−45°	45°
Δi_2 (x_2)	−45°	45°
$\Delta\theta_2$ (x_3)	0°	120°
$\Delta\theta_3$ (x_4)	0°	120°

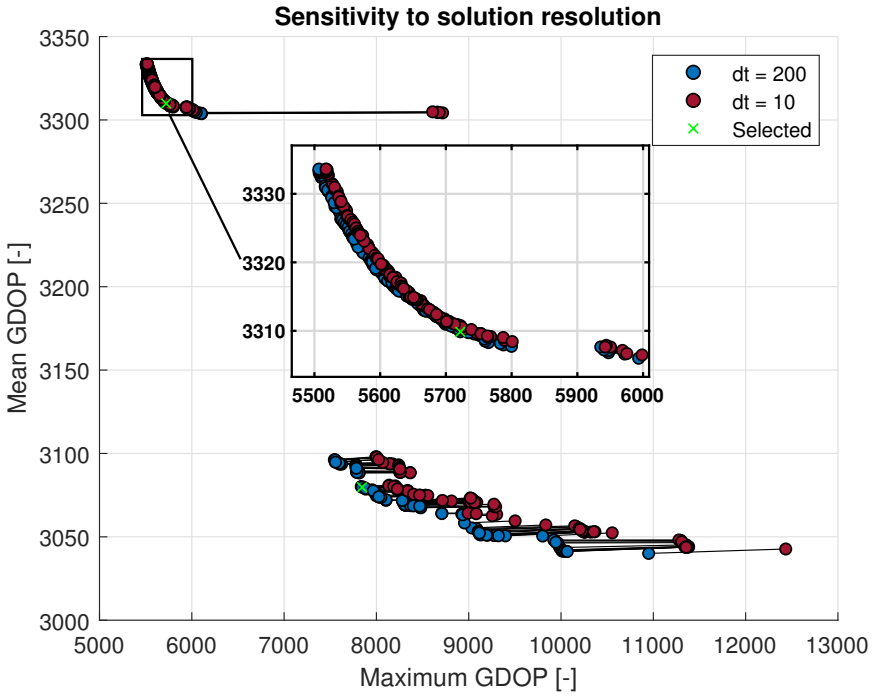

Figure 5.2: Pareto front as obtained from the optimization (dt=200), and a higher resolution rerun (dt=10). Two selected constellations are marked with *x*.

GDOP observed in the time series is used as second fitness value. Whenever a single-objective optimization algorithm is used, these two fitness values are linearly combined with equal weights.

5.2.3. Optimization method

For the constellation optimization, the Borg Multiobjective Evolutionary Algorithm (MOEA) has been used, which is developed by Hadka and Reed [2013]. This algorithm has been shown to outperform various other multi-objective methods at various tests. Thanks to its auto-adaptive properties, the challenge of tweaking the optimizer properties is greatly reduced when compared to non-adaptive optimizers. Moreover, its easy to use implementation in a Julia package called *BlackBoxOptim*, make it convenient to apply to the simulation at hand.

5.2.4. Optimization results

In order to obtain an optimized constellation, an optimization with Borg MOEA has been run with an initial population of 400 for approximately 20 000 function evaluations. From this, the Pareto front in Figure 5.2 is obtained. Figure 5.3 shows the relation between the mean GDOP fitness and the design parameters for these results.

The Pareto front is distinctly split into two fronts, one with a lower maximum GDOP value and a higher mean GDOP, whereas the second front has a lower mean GDOP yet a higher maximum. These groups can also be recognised as groups of clearly distinct input parameters. The front with higher mean GDOP all have a value for Δi_2 of near 45°, and will be referred to as the *skewed* solutions. The second group, with lower

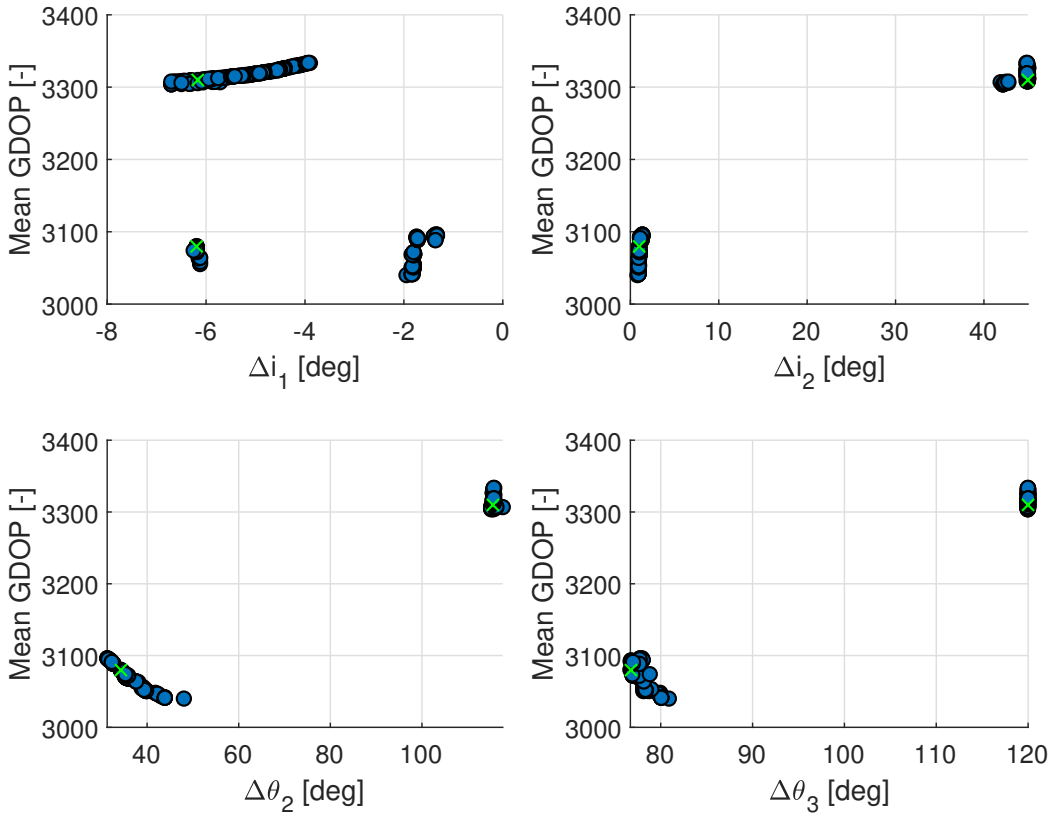

Figure 5.3: The optimization parameters of the Pareto front. The constellations are grouped as *level* for near-zero x_2 and *skewed* for near 45° values of x_2.

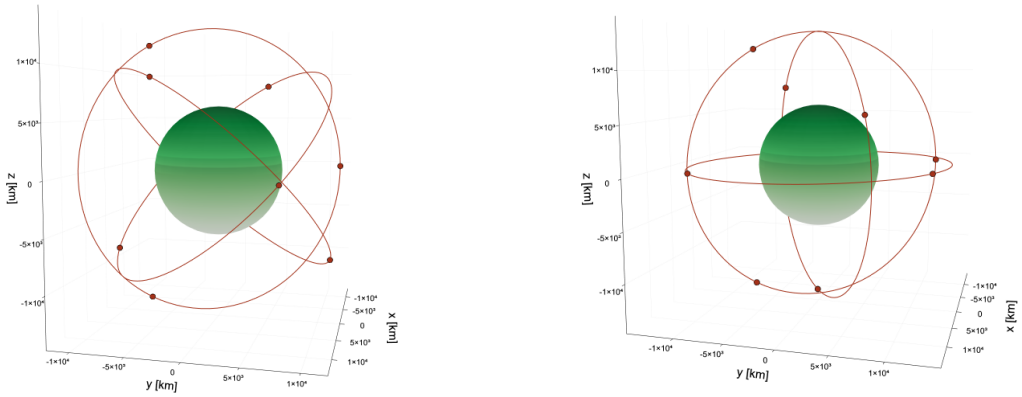

(a) A selected *skewed* constellation.

(b) A selected *level* constellation.

Figure 5.4: The two selected constellations as indicated in Figure 5.2. The x-y plane is the ecliptic plane of the Earth.

mean GDOP, have Δi_2 near 0°, hence will be referred to as the *level* solutions. For both groups, one individual has been selected based on its performance, and is visualized in Figure 5.4.

For both the skewed and the level solutions, Δi_1 is a few degrees negative. Considering the orbit of the Moon is inclined by 5.16° with respect to the ecliptic, the solutions of the first orbit all lie close to orthogonal to the ecliptic plane. Moreover, where the level solutions have the second plane near orthogonal to the ecliptic as well, whereas the third plane is near parallel to the ecliptic plane, the skewed solutions have both their third and second plane inclined by approximately 45 degrees with respect to the ecliptic.

As the optimization is performed with a rather rough sample spacing, at 200 s, this Pareto front has been reevaluated at a higher resolution of 10 s to investigate the sensitivity of the solution to the sample frequency. The red dots in Figure 5.2 show the fitness of a sample at increased resolution, connected to its original fitness with a black line. For both groups in the front, the samples at low mean GDOP show a high sensitivity to this sample space. Especially the skewed solutions show only a small sensitivity to the resolution, whereas the level solutions are much more sensitive. This sensitivity of the level solutions is explained by an interaction effect; when neither of the polar planes is close to orthogonal to the Moon, the overall GDOP is greatly increased due to the constellations smaller observed footprint, however, at this point, no eclipse of the polar satellites will occur. Moreover, eclipses of the polar satellites will occur simultaneously with an eclipse of an equatorial satellite. At this point, the location of the observer is still well off-normal from the other polar plane, resulting in very high values for the GDOP. With a smaller time step, shorter simultaneous eclipses will be observed, resulting in the observation of a double eclipse while further off-normal from the polar planes than with a larger time step.

For the skewed constellation type, these double eclipses can be largely removed, making the maximum GDOP much less sensitive to the resolution. All the skewed constellations that do show a significant sensitivity to the time step have their i_2 parameter around 42°, making the described interaction effect possible due to a slight timing change of the eclipses of orbital planes 2 and 3.

Furthermore, a Monte-Carlo simulation has been performed on this optimization problem to verify the convergence of the solution. Both the Pareto front and Monte-Carlo solutions can be seen in Figure 5.5. All Monte-Carlo samples are dominated by one ore more results on the Pareto front, which is an indicator of successful convergence of the solution.

The final constellation that has been selected from the Pareto front to be used for LuNNaC has a mean GDOP of 3311, and a maximum of 5729. This constellation is depicted in Figure 5.4a. The Kepler elements for the individual satellites for this constellation can be seen in Appendix B.

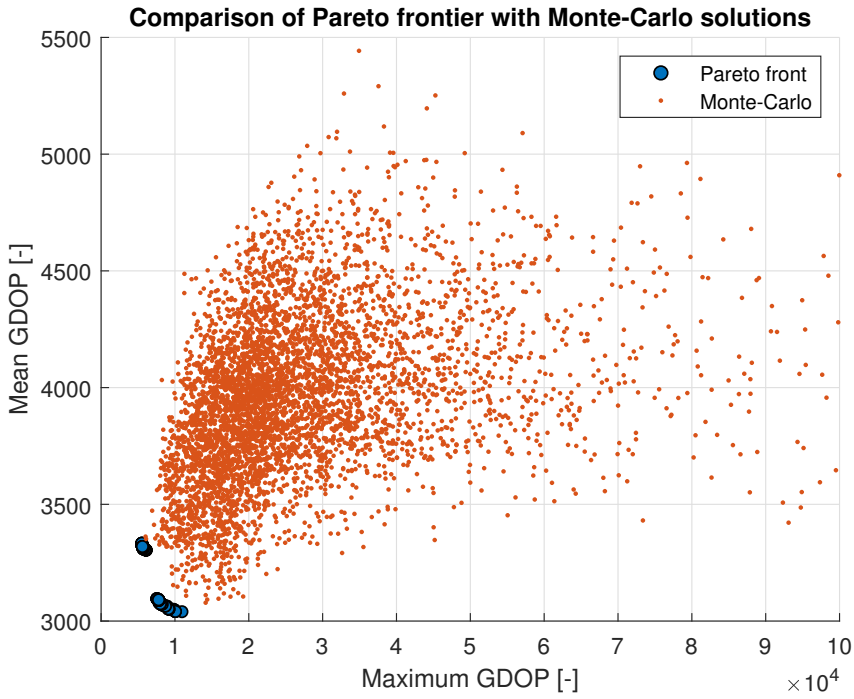

Figure 5.5: Comparison of Pareto front of the optimization of PECMEO navigation constellations with Monte-Carlo analysis.

5.3. Effect of omitting ionospheric observations

From the resulting LuNNaC constellation, the GDOP can be determined with and without inclusion of signals that travel through the ionosphere. This is then used to emphasize the effect of completely omitting ionospheric signals with respect to a case where perfect correction of the delays occur. Similar to the optimization, the Lunar orbit is used as reference point for the GDOP, which is determined throughout an entire orbital period of the Moon at time intervals of 10 s for both cases.

The difference in GDOP is only present right before or after a navigation satellite eclipses behind the Earths horizon. As a result, an effect is only observed on relative short time spans, and any observed difference must be a GDOP increase. Figure 5.6 shows this increase in GDOP in time. In 13.9% of the samples, an increase in GDOP has been observed. Of the samples that show an increase, the mean increase is 667, with a minimum of 101 and a maximum of 1625. The relative increase has a mean of 22.4%, a minimum of 4.9% and a maximum of 56.4%.

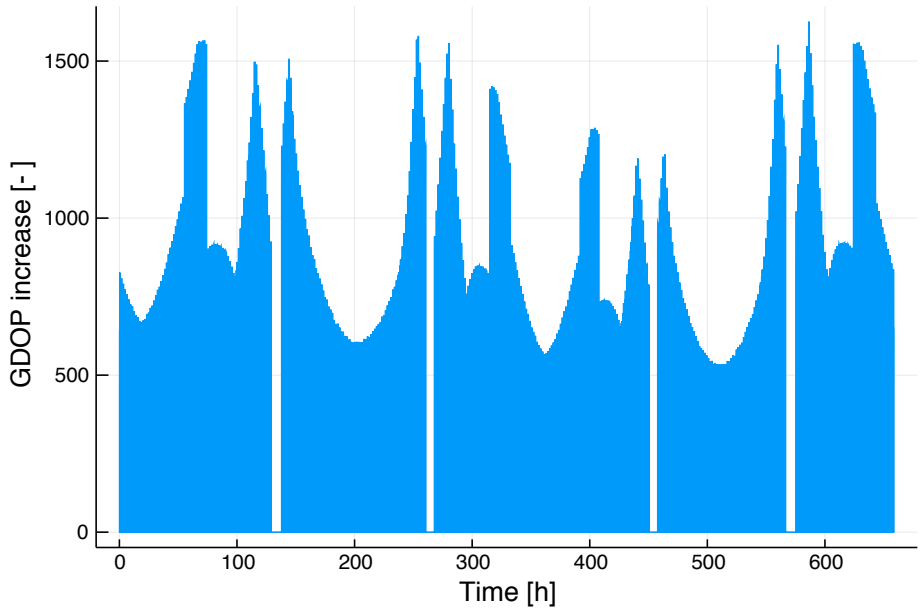

Figure 5.6: GDOP increase as a result of neglecting all signals passing through the ionospheric layer below $h = 800\,\text{km}$

6

Satellite position determination methods

In order to obtain spacecraft positions from the observations, navigation algorithms are used. This thesis works limits to two different algorithms, the point position least squares method, and the kinematic least squares method. Both of these use the iterative least squares method to find the model parameters to best fit the observations. Hence, the iterative least-squares will be explained first. Moreover, the point position and kinematic least squares methods are explained and obtained solutions will be shown. The following simulation cases using the low Lunar orbit, discussed in subsection 3.5.1, will be discussed in this chapter:

- Point position results
- Error free kinematic least squares
- Kinematic least squares with perfect ephemerides
- Kinematic least squares without observation noise
- Kinematic least squares with all error sources
- Real-time kinematic least squares solution

Each of these simulations are performed for a 96-hour arc. Observations are performed at a 30 s interval. The length of the simulation is chosen to obtain a large number of epoch updates, 192 of which occur in a 96-hour arc, in order to have a large sample size for the ephemeris errors. The simulation starts at the epoch of the Moon orbital parameters, which corresponds to J2000. During this simulation, the Moon is near the apogee of its orbit, and therefore, the Earth-Moon distance is relatively large when compared to the mean Earth-Moon distance. Moreover, the maximum GDOP value found in subsection 5.2.4 is also included in this arc. Therefore, this simulation arc can therefore be considered a worst-case scenario for both GDOP and observation noise.
Finally, one simulation case for a transfer orbit is discussed:

- Kinematic least squares for a satellite in transfer orbit

6.1. Non-linear least squares

The least squares method is used to find estimation parameters, $\vec{y}$, such that a model, $h(y)$, has the best fit on measurements z. Therefore, the goal is to find y, such that the sum of the squares of the residuals, seen in Equation 6.2, is minimized. The residuals are defined as the difference between observation data and model function, as given in Equation 6.1.

$$\vec{r}_i = \vec{z} - \vec{h}(\vec{y}) \tag{6.1}$$

$$S = \sum_{i=1}^{n} r_i^2 \tag{6.2}$$

When the least squares solution for a non-linear problem needs to be found, the non-linear least squares method, or iterative least squares method, must be used. For both the navigation code and carrier phase observation equations, seen in Equation 4.3 and Equation 4.7, this is the case. The scalar $\rho_r^s(t)$ term in these equations can be defined as $\rho_r^s(t) = |r^s(t-\tau) - r_r(t)|$, where r^s is the position of the navigation satellite, and r_r is the position of the receiver, and hence the model function has a non-linear dependency on the estimated parameters, which includes the receiver position vector.
Rather than directly solving for a closed form solution of the partial derivative of the model with respect to the parameters, an iterative approach is taken by linearization of h around an initial value y_0, in order to estimate an updated parameter $y_1 = y_0 + \Delta y$. Multiple iterations are used until convergence is achieved, which can be observed through the values in Δy. The update parameters can be found from Equation 6.3.

$$\Delta y = \left(H^T W H\right)^{-1} H^T W \left(z - h(y_0)\right) \tag{6.3}$$

Here, the weight matrix, $W = Q_z^{-1}$ ideally is the inverted covariance matrix of the observations. In reality, the inverse of estimated variances are used, as the actual observation covariances are not available during real-time navigation. Furthermore, the design matrix, H, is defined as the partial derivatives of the modeled measurements with respect to the estimation parameters; $H = \frac{\partial h(y_0)}{\partial y_0}$.

6.2. Point position estimation

The point position least squares method uses least squares on the code observations of a single epoch to obtain position and receiver clock correction estimates for that single epoch. The information used for the point position method is limited to pseudorange observations. As processing is done on an epoch-by-epoch basis, the information between epochs can not be interconnected, and as a result, the number of carrier phase measurements that could be added will be equal to the number of bias parameters that is estimated to find the integer ambiguity. Hence, the quality of position or clock error information is not improved by adding carrier phase measurements.

In order to obtain the point position estimation, the nonlinear least squares method is used, as explained in section 6.1. As model for the least squares, the observation equation for pseudoranges, seen in Equation 4.3 is simplified into Equation 6.4.

$$P_r^s(t) = \rho_r^s(t) + c\delta t_r(t) - c\delta t^s(t) \tag{6.4}$$

The transmitter clock errors, $\delta t^s(t)$, is assumed to be broadcasted and will therefore not be estimated. Furthermore, $\rho_r^s(t)$ is the geometric distance the signal has traveled from receiver to transmitter, and δt_r is the receiver clock error. The term ϵ_r^s, as seen in Equation 4.3 is assumed to be normally distributed with a zero mean, hence $\mathrm{E}[\epsilon_r^s] = 0$.
The estimated parameters are the 3D position (x, y and z), and receiver clock error, δt_r, the latter converted to meters through the speed of light. Hence, the parameter vector is $y = (x^s, y^s, z^s, c\delta t^s)$. The design matrix are the partial derivatives with respect to the parameters vector for each observation. This results in $H_i = (e_r^i, 1)$, where index i denotes the navigation satellite for which the receiver has a corresponding observation. Here, e, as seen in Equation 6.5 corresponds to the unit vector pointing from the receiver to the transmission location of the corresponding signal. Therefore, the transmitter position at time of transmissions ($r^s(t-\tau)$) has to be used, where τ is the time traveled by the signal as described in subsection 4.2.1.

$$e_r^s(t) = \frac{r_r(t) - r^s(t-\tau)}{|r_r(t) - r^s(t-\tau)|} \tag{6.5}$$

In this equation, $r_r(t)$ denotes the receiver position vector, and $r^s(t)$ represents the transmitter position vector. Furthermore, an identity matrix is used as weight matrix for the least squares ($W = I(4)$), as the noise levels of all received pseudorange signals will be roughly identical. Especially when compared to GPS, the relative variations in signal noise levels are much smaller for LuNNaC due to a more constant distance between transmitter and receiver.

Applying this point position least squares method to the generated observations, for an arc of 96 hours, with 30 second observation interval, yields a mean 3d position error of 14219 m. Hence, on itself it results in rather poor positioning. However, this low accuracy result is used as apriori for the Kinematic least squares method to improve its convergence.

6.3. Kinematic least squares

The kinematic least squares method is a batch least squares method for processing the navigation observations. Therefore, the information of a series of epochs, called an arc, is processed at once, allowing the carrier phase observations to be used alongside the pseudorange measurements. Due to the much lower observation noise on carrier phase observations, these are generally much more precise, and therefore, a higher navigation accuracy is achieved. The pseudorange observations, however, still are used in this kinematic algorithm, in order to ensure that $H^T H$ does not become singular.

The carrier phase observations contain an integer ambiguity term, which remains constant per passage of a satellite. By making only one estimation of this value while the satellite is observed, many high accuracy observations can be added at the cost of only a few extra estimated parameters. Meanwhile, the position and clock error estimation parameters remain disassociated in time. Therefore, no knowledge of the system dynamics or clock accuracy is assumed during the estimation process, which decreases complexity of the estimation process. Moreover, it makes the system more applicable for a real-time scenario where the system is undergoing accelerations with low predictability, such as a rover on the lunar surface, or a descent system with activated engines.

The estimation parameters are described by Montenbruck [2003] as Equation 6.6 and 6.7. Matrix Y contains a combination of receiver position and clock correction for each epoch, similar to the estimated parameters in the point positioning least squares method shown in section 6.2. Furthermore, B contains all bias estimations. The total number of estimated parameters is $4N + M$, where N is the number of epochs, and M is the sum of the number of observations passes for each navigation satellite. In a situation with a short arc, where no cycle slip or loss of track has occurred, this is equal to the number of satellites that have been observed.

$$\left(Y^T, B^T\right) = \left(y_1^T, ..., y_N^T, b_1, ..., b_M\right) \tag{6.6}$$

$$y_i^T = \left(r_{r,i}^T, c\delta t_{r,i}\right) \tag{6.7}$$

These estimation parameters yield least squares equation as seen in Equation 6.8. Here, H is the design matrix, W is the weight matrix, and z are the observations. Furthermore, $h(Y_i, B_i)$ are the modeled observations for iteration i, and ΔY and ΔB are the update vectors for the per-epoch quantities (Y) and the estimated biases (B).

$$H^T W H \begin{pmatrix} \Delta Y \\ \Delta B \end{pmatrix} = H^T W \left(z - h(Y_i, B_i)\right) \tag{6.8}$$

The model used for the pseudorange observations is as shown in Equation 6.9. Furthermore, the model applied to carrier phase observations is shown in Equation 6.10. ρ_r^s is the range between transmitter and receiver, corrected for light time effect. This is dependent on time, t, and the parameters y_i, where $i(k)$ is the epoch corresponding to observations k, and used to select the subset of parameters from Y. b_m is the bias value corresponding to the observation, where $m(k)$ is the bias index corresponding to observation k.

$$h_{PR}^k(Y, B) = \rho_r^s(t, y_{i(k)}) + \delta t_r(t) - \delta t^s \tag{6.9}$$

$$h_\phi^k(Y, B) = \rho_t^s(t, y_{i(k)}) + \delta t_r(t) - \delta t^s - b_{m(k)} \tag{6.10}$$

This yields the partial derivatives for the observation equation with respect to the position and clock correction parameter vectors for the various epochs j, for observation k, as seen in Equation 6.11. Furthermore, Equation 6.12 is the partial derivative for the carrier phase observation model with respect to the various bias values b_j. Here, δ is the Kronecker symbol, where $\delta_{i(k),j} = 1$ only when $i(k) = j$, and is 0 for any other case, ensuring that the observations only have an influence on the parameters of the corresponding epoch, and on the correct bias values. Moreover, e_k is the line of sight vector as explained in section 6.2.

$$\frac{\partial h_k}{\partial y_j} = \delta_{i(k),j} \cdot \left(e_k^T, 1\right) \tag{6.11}$$

$$\left[\frac{\partial h_k}{\partial b_j}\right]_\phi = \delta_{m(k),j} \cdot (-1) \tag{6.12}$$

6.3.1. Block elimination

One of the challenges of the kinematic least squares method is the scaling with number of epochs of the computational cost required for calculation of $\left(H^T W H\right)^{-1}$. Due to the definition of the partial derivatives of the observations Kronecker symbols, then normal matrix $N = \left(H^T W H\right)$ is very sparse. By splitting the X and B components for the least squares equation, Equation 6.8 becomes Equation 6.13.

$$\begin{pmatrix} N_{XX} & N_{XB} \\ N_{BX} & N_{BB} \end{pmatrix} \begin{pmatrix} \Delta X \\ \Delta B \end{pmatrix} = \begin{pmatrix} n_X \\ n_B \end{pmatrix} = \begin{pmatrix} H^T W(z - h(X,B)) \\ H_B^T W(z - h(X,B)) \end{pmatrix} \tag{6.13}$$

Here, N_{XX} and N_{BB} are sparse matrices, of which N_{XX} consists of a diagonal matrix of 4x4 matrices, and N_{BB} is a purely diagonal matrix. Furthermore, each sub-matrix of the normal matrix N can be calculated through matrix multiplication $N = H^T W H$ for each sub-matrix. However, each of the N sub-matrices can also be constructed directly by using the knowledge that each observations only limits a few parameters, and thus spaces in the N matrix.
Firstly, when solving the least squares equation, N_{XX}^{-1} must be known. The cost of this inverse can be greatly reduced by inverting the individual sub-matrices for each epoch using Equation 6.14, where blk-diag stands for the block diagonal matrix of the given matrices.

$$N_{XX}^{-1} = \text{blk-diag}\left(N_{XX,1}^{-1}, ..., N_{XX,N}^{-1}\right) \tag{6.14}$$

Here, the sub-matrices of N_{XX} are calculated by summing over the observations using Equation 6.15. In this equation, e_k is the line-of-sight vector for observation k, W_k is the weight for observation k, and j is the epoch for which the sub-matrix is to be calculated.

$$N_{XX,j} = \sum_{i(k)=j} \begin{pmatrix} e_k \\ 1 \end{pmatrix} (e_k, 1)\, W_k \tag{6.15}$$

This procedure so far has been described previously by Montenbruck [2003]. However, the remaining blocks of matrix N can also be constructed in a direct fashion, which is found to be much more computationally efficient than constructing these matrices through direct matrix multiplication of design matrices.
Firstly, N_{BB} can be constructed through Equation 6.16. Here, then values for the diagonal are found using Equation 6.17, which is a series over all carrier phase observations. j is used as iterator for bias indices, and $m(k)$ is the bias index corresponding to observation k.

$$N_{BB} = \text{blk-diag}\left(N_{BB,1}, ..., N_{BB,M}\right) \tag{6.16}$$

$$N_{BB,j} = \sum_{m(k)=j} W_j \tag{6.17}$$

Finally, the sub-matrices linking the per-epoch parameters to the bias parameters are N_{XB} and N_{BX}. Firstly, it should be noted that only one of these has to be constructed, as $N_{BX} = N_{XB}^T$. Now, this matrix can be constructed using Equation 6.18, where the summation should be performed over the carrier phase observations. Here, j_e indicates the row of the N_{XB} matrix, while j_b indicates the column.

$$N_{XB,j_e,j_b} = \sum_{i(k)=j_e \& m(k)=j_b} -\begin{pmatrix} e_k \\ 1 \end{pmatrix} W_k \tag{6.18}$$

Now the least squares solution for Equation 6.13 must be split into two parts as well, firstly for the bias parameters, after which the per-epoch parameters can be calculated. First, the update parameters ΔB is calculated using Equation 6.19, after which the update for the position and clock error parameters is calculated using Equation 6.20.

$$\Delta B = \left(N_{BB} - N_{BX} N_{XX}^{-1} N_{XB}\right)^{-1} \times \left(n_B - N_{BX} N_{XX}^{-1} n_X\right) \tag{6.19}$$

$$\Delta X = N_{XX}^{-1} \left(n_x - N_{XB} \Delta B\right) \tag{6.20}$$

Furthermore, the covariance matrices can be calculated using Equation 6.21, and Equation 6.21. From the latter, the formal position accuracy can be calculated. This is performed by separating 4x4 blocks on the diagonal for each epoch, and taking the RSS of the first three diagonals on in this block.

$$Q_{BB} = \left(N_{BB} - N_{BX}N_{XX}^{-1}N_{XB}\right)^{-1} \tag{6.21}$$

$$Q_{XX} = N_{XX}^{-1} + \left(N_{XX}^{-1}N_{XB}\right)Q_{BB}\left(N_{XX}^{-1}N_{XB}\right)^{T} \tag{6.22}$$

6.3.2. Kinematic LSQ estimation weights

Ideally, the weight matrix is defined by the inverse of the covariance matrix of the observations, given by $W = Q_z^{-1}$. However, as the variances due to measurement noise within a single observation type differ little, especially for low Lunar orbits as has been in shown in section 4.3, and their exact values are not always known for a real receiver, constant weights are used for both pseudorange and carrier phase observations. Besides measurement noise, the ephemeris errors also have an influence on the error of the observation with respect to the model. When assuming the ephemeris error results in a normally distributed measurement error, with a zero mean, the ideal weight for an observation becomes Equation 6.23, which is the addition of the variance due to measurement noise and the variance of error due to ephemeris errors.

$$W_i = \left(\sigma_i^2 + \sigma_{eph}^2\right)^{-1} \tag{6.23}$$

The values for standard deviations used to find the constant weights are $\sigma_{eph} = 0.01\,\text{m}$ for ephemeris error, $\sigma_{PR} = 6.5\,\text{m}$ for pseudorange, and $\sigma_\phi = 0.0015\,\text{m}$. This yields a weight $W_{PR} = \left(6.5^2 + 0.01^2\right)$ for all pseudorange observations, and $W_\phi = \left(0.0015^2 + 0.01^2\right)$ for the carrier phase observations.
Moreover, it should be noted that taking the ephemeris error into consideration for the value of the weights has a very small influence on the mean RSS position error obtained. A 96 hour simulation, with 30 seconds interval between observations shows a mean position error of 27.0 m. By including the ephemeris error the relative weight of the phase observations with respect to pseudorange observations is reduced by a factor 45. The mean error, however, increases by 0.6 mm, and therefore is negligible with respect to the individual errors. This reduction is explained by the ephemeris component in the error not being an independent variable between observations, which is an assumption made when using its variance as component in the weight. On the other hand, the inclusion of ephemeris error in the weights ensures a more realistic formal error is obtained.

6.3.3. Solution arc splitting

The presented LuNNaC system comprises only of medium altitude Earth orbiting satellites, which results in a lack of coverage on the far side of the moon. Therefore, a satellite in Lunar orbit, equatorial Lunar orbits in particular, will find itself losing track of all navigation satellites at some point in its orbit. For these epochs, no position estimation is possible with either point position or Kinematic method, as both methods need a minimum of 4 observations per epoch. Moreover, after the eclipse all bias values need to be re-estimated as the integer ambiguity values for the carrier phase observations will have changed from their values prior to the eclipse. This results in a complete numerical disconnection between the navigation solutions before and after the eclipse. As a result, the same solution is obtained when splitting the solutions in multiple arcs which are individually solved using the Kinematic least squares method. Montenbruck [2003] indicates that the count of arithmetic operations is proportional to $M^2(4N)$, where M is the number of estimated bias parameters and N the number of estimated epochs. Hence, when the overhead is small it can computationally be much more efficient to calculate these arcs separately. Moreover, when these eclipses occur sufficiently often, no arc splits withing satellite passes are needed.

6.3.4. Error free Kinematic LSQ solution

As verification of the Kinematic least squares method, a simulation has been performed where the observation noise has been set to zero, and no ephemeris errors are induced. The resulting accuracy for the first 8 hours of the 96 hours arc is seen in Figure 6.1. The mean position error from the kinematic least squares solution is $8.4 \times 10^{-5}\,\text{m}$. Hence, without the influence of errors in navigation or ephemeris, a near-perfect solution can be found using the kinematic least squares, even though still under the presence of clock errors of up to 61 m. Similar to the simulation case with noiseless observations, the point position

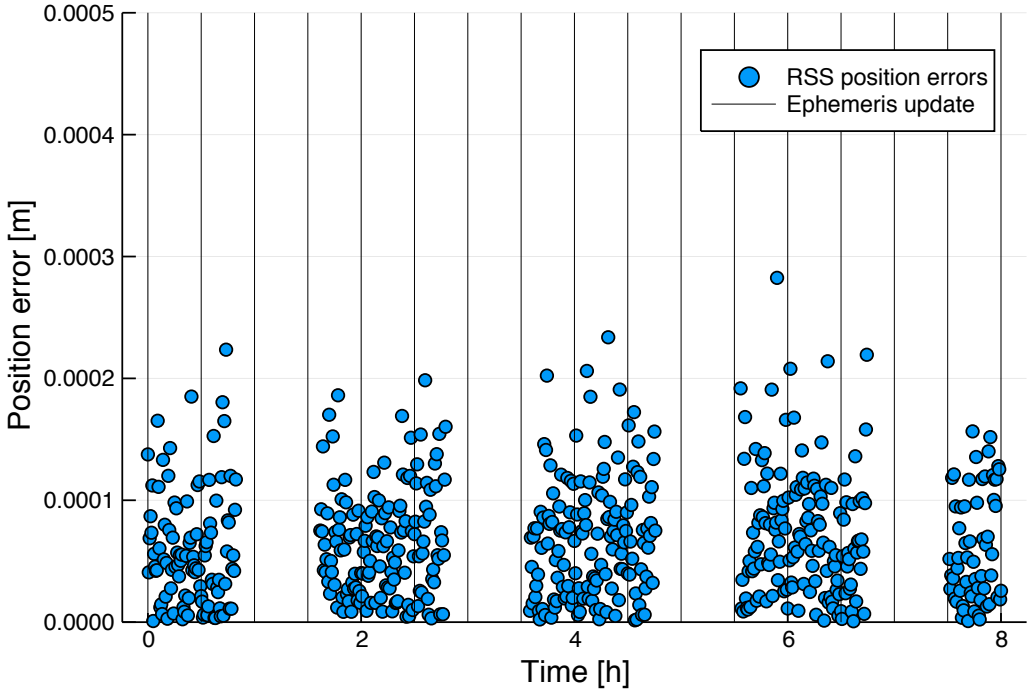

Figure 6.1: Navigation errors for a low Lunar satellite without noise and ephemeris errors using the kinematic least-squares method.

least squares slightly outperforms the kinematic least square, as the former has a mean position error of 7.8×10^{-5} m.

6.3.5. Perfect ephemeris Kinematic LSQ solution

The first step up in complexity from the error free case, is a simulation case where only observation noise is considered, but with perfect ephemerides. The first 8 hours of the full 96 hour simulation for such a case can be seen in Figure 6.2. In this case, the obtained position errors are random, and no clear systematic errors are present in the solution. Occasionally, the first or last solution of a solution arc has a much higher error. This is caused by an increase in GDOP when the receiver is behind the Moon for only part of the transmitters, allowing a solution to be found, albeit of lower quality. The mean position error for the kinematic solution is 3.3 m. The point positioning solution for such a simulation case has a mean position error of 14.2 km, clearly showing the benefit of including the carrier phase observations, which have a much higher precision.

6.3.6. Noiseless Kinematic LSQ solution

Similarly, a simulation case has been performed where the observations are noiseless, yet ephemeris errors are included. For this, the results are shown in Figure 6.3. In this case, the mean position error for the kinematic solution is 26.8 m. This is a considerably higher mean position error than in the noise-only case, and therefore, the ephemeris error clearly is the dominant error source when carrier phase observations are included for the solution.

When considering the position error against time, the error generally changes smoothly. This smooth, yet not constant error profile is caused by the ephemeris errors changing with propagation of the navigation satellite, as discussed in subsection 2.2.3. Two causes for discrete changes in position error can be identified. Firstly, whenever the signal of a navigation satellite is lost due to blockage of this signal by the Moon or Earth, the GDOP changes discretely, causing a change in position errors. This occurs for short time spans within arcs, but is also visible at the start and end of observations arcs, where significantly larger errors can be observed. Moreover, when the ephemerides are updated, once every 30 minutes, and thus the ephemeris errors change, a discrete in position errors occurs as well.

The mean error for the point positioning solution for the corresponding observations is in this case 22.9 m, which is better than the corresponding kinematic solution. In this case, pseudorange observations are not of lower quality than carrier phase observations. When including the latter in the solution, however, adds the

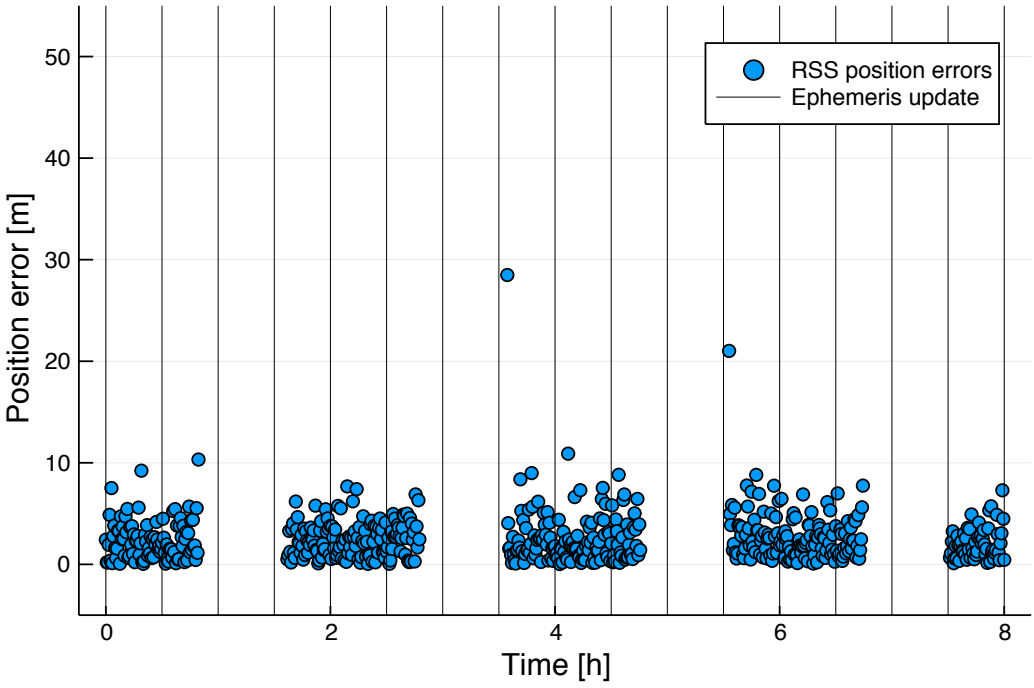

Figure 6.2: Navigation errors for a low Lunar satellite, with perfect ephemerides.

need to estimate the ambiguities, which increases the errors in the solution.

6.3.7. Complete Kinematic LSQ navigation solutions

Finally, a simulation case is run where both ephemeris errors and measurement noise are included. The observation errors are ensured to be identical to those in the noise-only case, and the ephemeris errors are identical to those in the noise-free case shown previously. For the first 8 hours of this solution the RSS position errors are shown in Figure 6.4, together with the formal accuracy and the times at which ephemeris updates occur. For the full arc, the Kinematic least squares results in a mean 3d position error of 27.0 m. The Kinematic least squares solution for such an 96 hour arc takes approximately 75 s to solve on an i7-2600K CPU.

Firstly, it should be noted how many of the RSS position errors from sequential epochs group around a similar position error. This is caused by the ephemeris error which is greater in magnitude than the carrier phase errors. Hence, a small change in time results only in minor changes in navigation constellation geometries and a very similar ephemeris error, resulting in a similar base error level. The measurement noise causes for variation around this base error level. Furthermore, these similar errors suddenly change in magnitude upon an ephemeris update, which confirms that this is indeed caused by ephemeris errors.

Due to these groupings, the formal error is, especially for short time spans, a rather weak estimator for position error magnitude. In the complete 96 hour data set, however, the formal position error exceeds the RSS position error in 55.5% of the samples, which becomes 90.2% when doubling the formal error (2σ), and 97.0% when tripling (3σ). This is on the low side for a good fit on a normal distribution due to the mean standard deviations for phase and carrier errors being above the corresponding values used for the weights. In other words, the constant standard deviation for the observation noise, used to determine the weight, is underestimated in this arc, as these 96 hours occur when the Moon is relatively far from earth with respect to its mean. As a result, the formal position error is underestimated.

Furthermore, peaks in both the error in position solution, as well as in formal accuracy are observed for the first and last few epochs for each arc. Due to the difference in location of the navigation satellites, the receiver will lose contact to them one by one when it moves behind the surface of the Moon. Therefore, right before and after this eclipse, the quality of the solution can rapidly deteriorate due to having contact to fewer satellites, as this not only reduces the number of observations for the epoch, but can greatly reduce the GDOP. As this mainly is an effect on GDOP, it is not tied to a specific error type, and hence has also been shown to be present in both runes with isolated error sources.

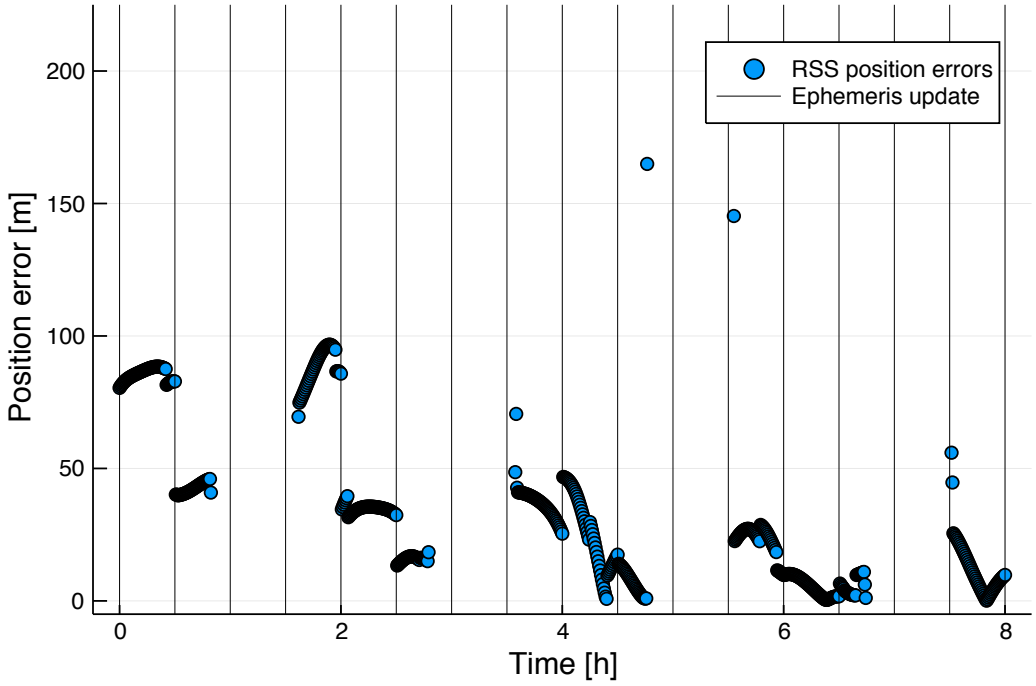

Figure 6.3: Navigation errors for a low Lunar satellite with noiseless observations using the kinematic least squares method. Ephemeris errors are included.

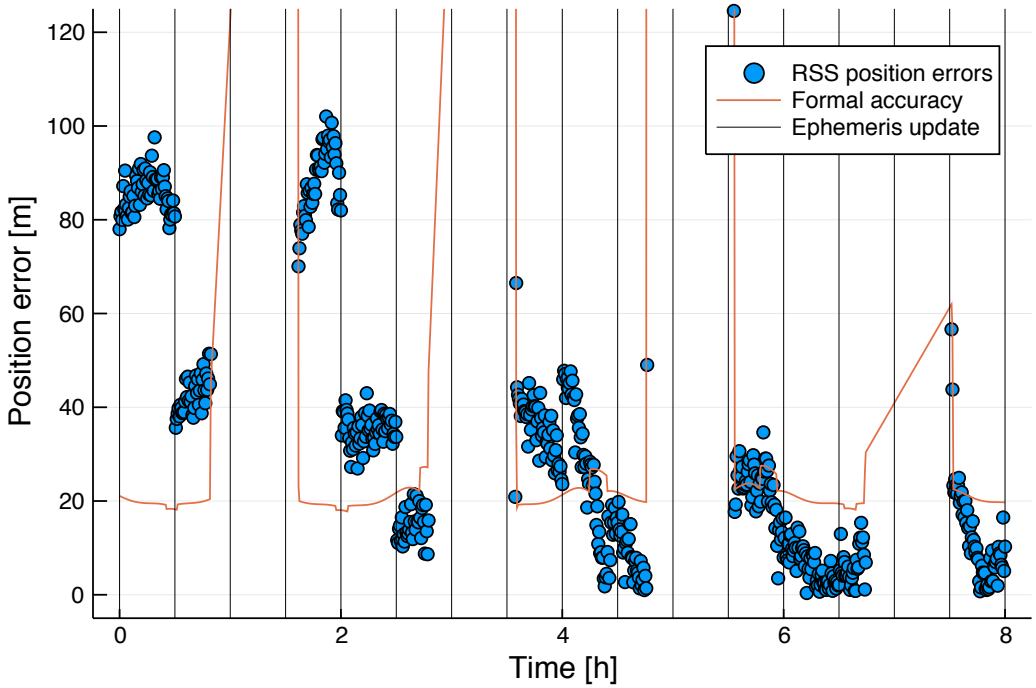

Figure 6.4: Navigation errors for a low Lunar satellite, including observation noise and ephemeris errors using the kinematic least squares method.

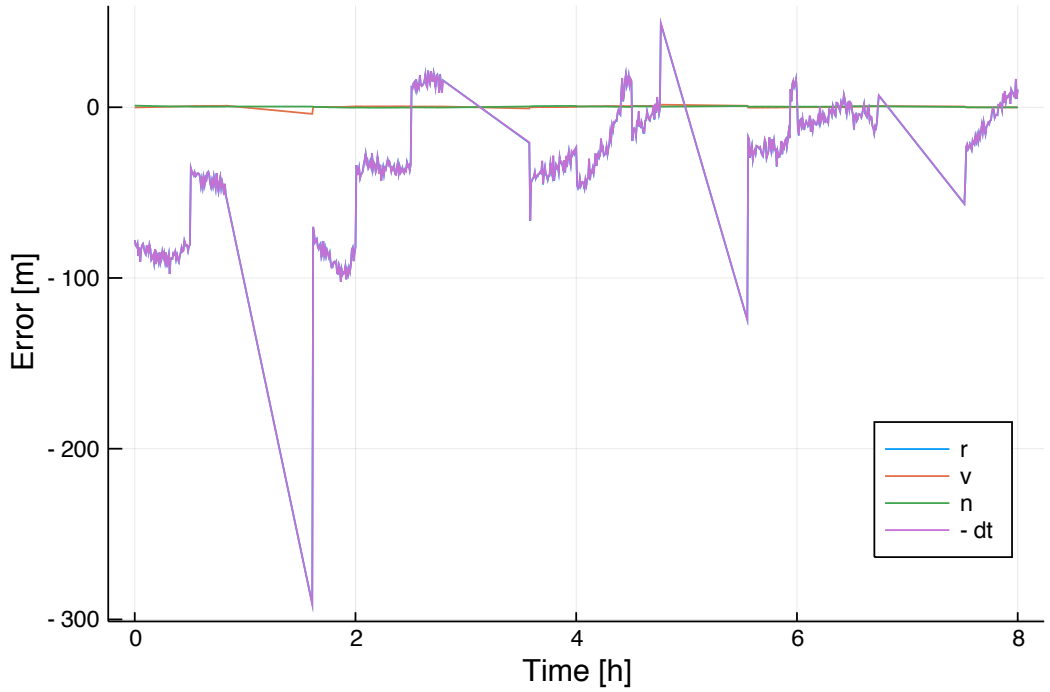

Figure 6.5: Navigation errors for a low Lunar satellite

Figure 6.5 shows the navigation errors divided into four components. The errors are projected in an rvn reference frame, where r is the radial vector pointing towards the Moon, v, is the in-orbital-plane vector components orthogonal to r. Finally, n is normal to the orbital plane of the Moon. The dt error represents the error in estimation of the clock correction parameter. Clearly, a strong correlation is observed between the errors in r and dt. The covariance between these error components is -0.999988. Especially due to the poor geometry, errors in the r and dt component in the observation model result in roughly the same change, resulting in such correlation. The covariances between the three position error components are all in the range -0.06 between r and v, to .22 between v and n. Hence, these position errors are much less correlated.

6.4. Real-time kinematic least squares

As the kinematic navigation solution shown in section 6.3 is a batch least squares method, processing all epochs simultaneously, it is most conveniently used as a post-facto processing method. In order to process the observations in real time, the solution for all epochs of the arc must be recalculated for each additional set of observations that is added. Therefore, it might be computationally more intensive than, for example, an extended Kalman filter, where a propagation and an update step are applied for each observation epoch, requiring only to process the most recent observations. On the other hand, the kinematic least squares method eliminates the need for knowledge about system dynamics, which can be convenient in a real-time on-board case, if such knowledge is not accurately available.

6.4.1. Real-time kinematic LSQ navigation solutions

The discussed Kinematic least squares method is adapted to simulate results that could be obtained in real time. For the solution at a given epoch, the arc is processed using all observations up to, and including the epoch. As a result, due to the availability of very limited data, the first few solutions of an arc in the real-time kinematic method have very poor accuracy. Generally, after a few observations, the position error drops below 100 m. On the other hand, as seen in Figure 6.6, it can also occur that after a few dozen observation epochs, the solution has not yet converged to a level below 200 m when, at that time, the ephemerides are poor. The reason behind the large difference in convergence of the solution is explained by the ephemeris errors and their updates. When solving an entire arc with the kinematic least squares, the arc span over several ephemeris updates for the transmitting satellites. As a result, a relatively poor ephemeris quality near the end of an arc will also influence the solutions at the start of the arc through the bias parameters. Vice versa, when

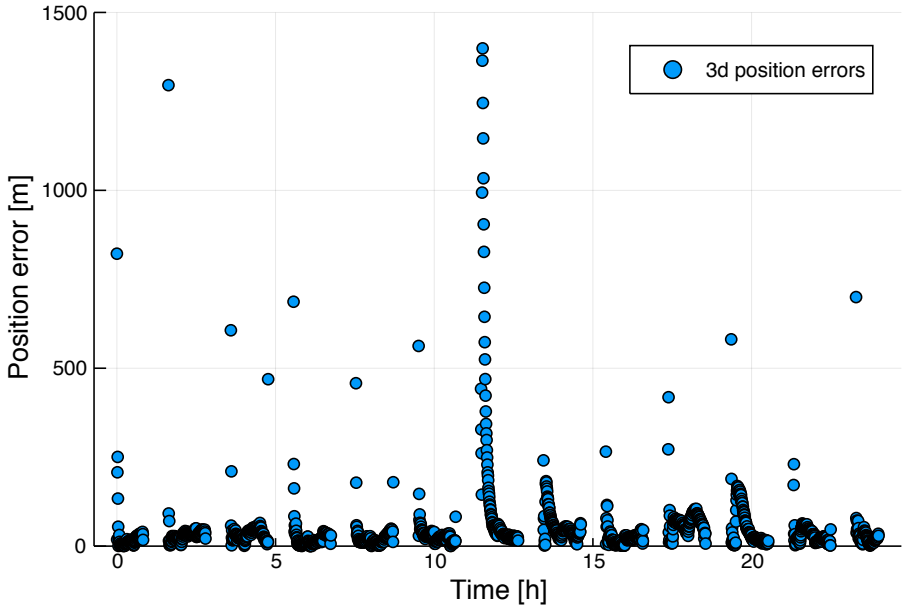

Figure 6.6: Real time solution obtained using kinematic least squares method.

an arc starts with relatively high quality ephemerides, the solution will converge to a level of position error below what is found when processing the entire arc.
When omitting the first 10 solutions of all arcs, the mean 3d position error for the real-time kinematic solution is 38.3 m, with a sample standard deviation of 61.1 m.

6.5. Navigation in transfer orbit

A simulation of navigation observations for a spacecraft in Hohmann transfer as described in subsection 3.5.2, with an observation interval of 2 minutes. Setting an arrival time of 800×10^3 s after the initial epoch t_0, the transfer starts at the perigee of the orbit at $t = 357 \times 10^3$ s, and the sphere of influence of the moon is entered at approximately $t = 72 \times 10^5$ s, at which point the simulation is stopped. Figure 6.7 shows the number of satellites that are tracked by the receiver during the Hohmann transfer as the receiver moves into the field of view of the transmitters. Navigation signals are only received just over two hours before entering the Hill sphere of the Moon. This short period of reception during the transfer is caused by the focus of the navigation signals on the Moon, as well as by assuming a signal cutoff after 10° antenna angle, as established in subsection 2.2.2.
When the number of tracked satellites reaches 4, and 4 observations are performed per observation epoch, a navigation solution can be obtained using the Kinematic method. The post-facto solution for this transfer is seen in Figure 6.8. Throughout this solution, a mean RSS position error of 23.9 m is found. However, it should be mentioned that the solution arc is quite small, with only a few ephemeris updates. Therefore, the number of samples for random ephemeris errors is quite small, resulting in a large dependency on the ephemeris error values on the actual errors. Independent of the ephemeris errors, however, is the formal accuracy. At the start of the solution, when only a few satellites are received, this is much higher than when all satellites are in sight. This is explained by the increase in GDOP that is obtained from receiving less satellites. The lower number of observations per epoch also makes the individual solutions more sensitive to ephemeris errors. This can be seen by the increase in position errors at the start of the solution, when observations from the 5th satellite are made, worsening the solution accuracy due to the ephemeris error for this satellite. Moreover, the sudden change to a much lower error level after the first ephemeris update after the start of signal reception further highlights that this is an effect of ephemeris errors.

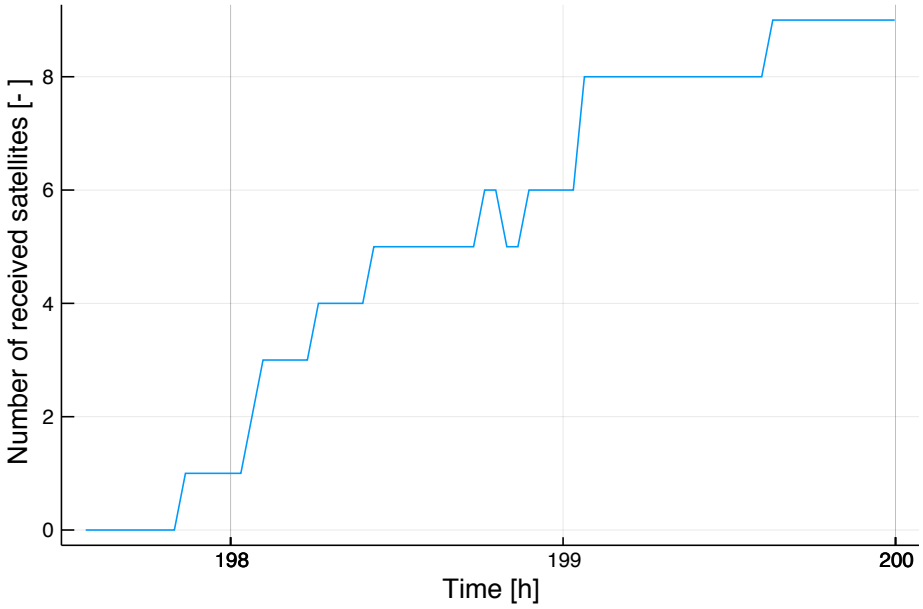

Figure 6.7: Number of tracked navigation satellites in a Hohmann transfer.

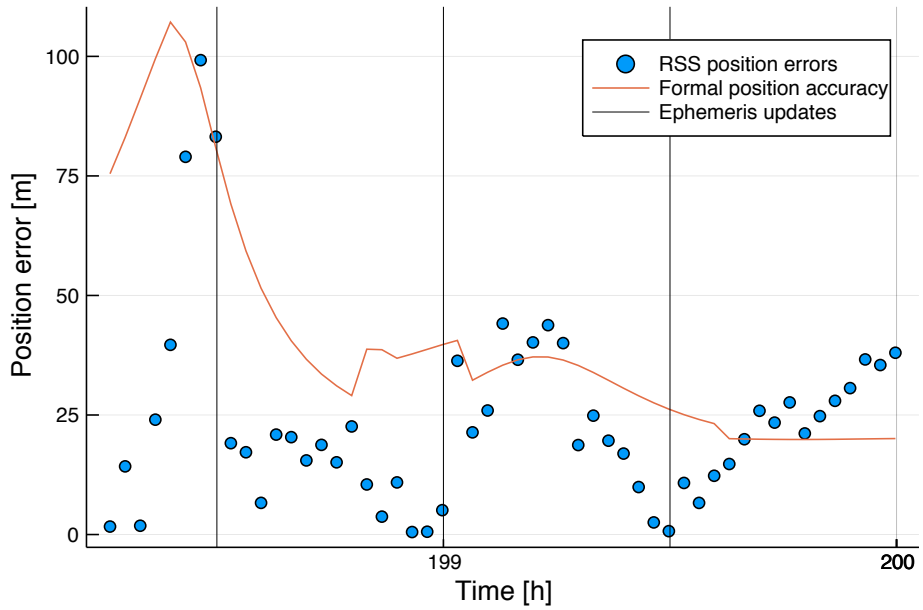

Figure 6.8: Navigation errors for Kinematic algorithm applied to a transfer orbit.

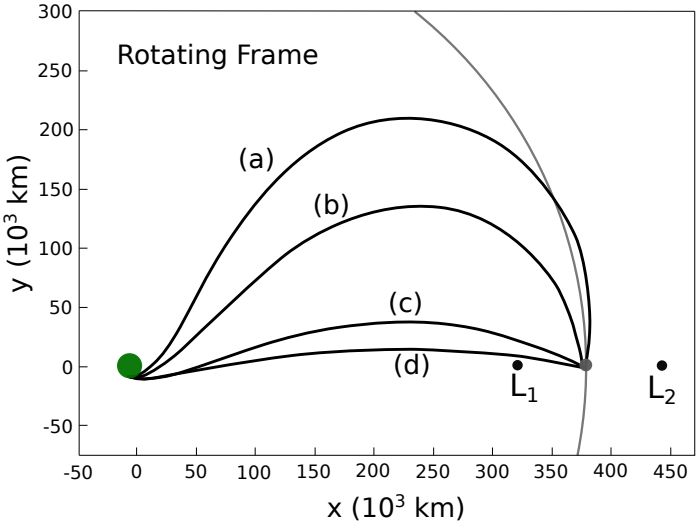

Figure 6.9: Depiction of low energy and high energy transfer orbits, based on Parker and Anderson [2014].

The flight paths for several spacecraft in a co-rotating reference frame, where the x-axis follows the Moon, is shown in Figure 6.9, based on work by Parker and Anderson [2014]. The path of the Hohmann transfer is between trajectory (a) and (b). From this figure, it becomes obvious how most of the transfer is spent at an angle with respect to the Moon that is well beyond 10°, and thus no signal is received. When reception of navigation signals is desirable, various adaptations can be made. Firstly, a wider main lobe will allow for more often reception of the signals during transfer. This will, however, result in a tremendous increase in the requirement of transmit power on the navigation satellites, especially when considering that the antenna beam half-angle must be increased to almost 38° to cover most of the transfer. Alternatively, the entire main beam of the transmitter antenna will have a smaller gain, resulting in a lower C/N_0. A second option involves designing the transmitter antenna to have side lobes at around 38°. This might provide a Hohmann transfer with enough coverage to find a navigation solution for a mid-course correction. This will, however, result in a solution that is very specific to Hohmann transfers, and might not provide sufficient coverage for other transfer orbits, such as free-return trajectories. Finally, when considering transfer orbits, usage of a high energy transfer might be considered when maximization of navigation signals is desirable. When further considering the orbits from Figure 6.9, transfer orbits between (d) and (e) are covered by the LuNNaC beams most of the duration of the transfer.

7

Conclusions and Outlook

The primary purpose of this research has been to assess the navigation accuracy of a spacecraft near the Moon using a PECMEO constellation. This research has been further subdivided into four parts, with the purpose of finding a high performance PECMEO constellation, and assessing the effect of observation noise, ephemeris errors and ionosphere. Here, the posed sub-questions will be answered, followed by the answer on the main research question. Finally, some recommendations for continuation on work on Lunar PECMEO navigation will be made.

Conclusions

As a first step of the research, a PECMEO constellation with an orbital radius of 14 000 km has been optimized based on maximum and mean GDOP throughout a full orbit of the Moon. Two rotation angles and two inter-orbit phasing angles have been used as optimization parameters. From the Pareto front, a constellation with its "equatorial" orbit in a plane close to ecliptic has been selected due to its low GDOP peaks and little sensitivity to simulation time resolution. When assuming the Moon as reference point for GDOP calculations, the selected constellation has a mean GDOP of 3311 and a maximum GDOP of 5729.

A major design decision for the LuNNaC constellation is whether to broadcast the navigation signal on multiple frequencies, allowing ionospheric free combination to be made, or to limit the system to a single frequency. When using only a single frequency, signals passing through the ionosphere are considered unusable for navigation, and are omitted. For the designed constellation, in approximately 14% of the epochs at least one observation is omitted. From this, an increase in GDOP of up to 56.4% is observed. With this combination of only a small percentage of epochs influenced, and albeit large, a not overwhelming increase in GDOP, it is considered that a single-frequency system would indeed be viable for the lunar navigation system.

A simulation of pseudorange and carrier phase observations has allowed the investigation of the effect of ephemeris errors and observation noise on the navigation solution. The standard deviation of the ephemeris errors is assumed to be 1.0 cm along 3 directions. Moreover, observation noise is determined using the link budget, resulting in a nominal standard deviation for the code observation noise of around 6.5 cm, and 1.5 mm for the carrier phase observations. The exact values for this noise change due to a changing signal travel distance as navigation satellites and the receiving spacecraft move in their orbits. In order to calculate the navigation solution, the kinematic least squares method has been used, with one constant weight for pseudorange and another for carrier phase observations. The results of these individual simulations is summarized in Table 7.1. The ephemeris errors result in a much larger navigation error than the carrier phase noise. From these results, a mean 3d position accuracy of ≈ 30 m can be achieved using the LuNNaC system. When compared to other Lunar navigation systems, this is around the same order of accuracy that can be achieved using ground based observation, but at higher altitudes. Furthermore, the accuracy of the system is by far good enough to be used for an Apollo like mission, with similar navigation requirements.

Table 7.1: Results for the mean position errors of the Kinematic navigation solution for various simulation cases.

Simulation case	Mean 3D position error
No noise or ephemeris error	8.4×10^{-5} m
No ephemeris error	3.3 m
No Noise	26.8 m
Noise + ephemeris errors	27 m

Recommendations

For continuation of the research work, firstly, one of the major uncertainties must be tackled, which is the magnitude of ephemeris errors. Is has been shown that ephemeris errors has the greatest contribution to the navigation error when using both carrier phase and pseudorange observations in a Kinematic method. The assumption made for the magnitude of the ephemeris error, however, is rather crude. Hence, to improve the certainty of this assumption, and thus the certainty of the correctness of the outcomes, the navigation capability of the navigation satellites should be investigated, from which an accuracy of the ephemerides can be assessed.

Moreover, the assumption for the orbital radius of the PECMEO navigation is not sufficiently justified to give certainty for it being the most desirable orbital radius. Although being a balance between high altitude, for a better geometry, and low altitude, for improved ephemeris accuracy, the trade-off between those has not been made due to a lack of knowledge about the ephemeris accuracy for varying altitudes. Hence, after assessment of navigation satellite altitude, a trade-off for altitude should be reconsidered while comparing altitude dependency of GDOP and the altitude dependency for the ephemeris errors, while also considering other constraints such as ensuring that the navigation satellites remain outside of the van Allen belts. Furthermore, when this yields an optimal altitude different from that used for PECMEO satellites in this research, the optimization should be reconsidered.

Furthermore, the constellations that have been found during the optimization seem to suggest that the inclined orbits have a larger contribution to the geometry improvement than the near-equatorial orbits. Therefore, it should be investigated if PECMEO constellations, or constellations with three orthogonal axes, are indeed optimal for usage in this Lunar navigation. From the results seen in the optimization, and especially the large GDOP peaks for the PECMEO constellation described as *level* in Figure 5.2.4 the following is suggested: A constellation with 3 orbits at equal inclination i, for which the right ascension of the ascending nodes and descending nodes is spaced equally. This constellation gives the opportunity for three polar orbits, where the Moon positions between geometry optima decreases, ensuring a more continuous low GDOP. Besides the interest in potential improved GDOP for such a constellation, one could investigate how the GDOP scales with increasing the number of orbits, which is not possible when staying with purely orthogonal orbits, yet likely has a larger impact than increasing the number of satellites per orbit.

Another option for improving the GDOP of the constellation is to add extra transmitters to the system in order to improve the navigation geometry. This can be realized in various ways, such as adding a transmitting beacon in Lunar orbit, or positioning a transmitter on the near-side of the Moon on the surface. A Lunar satellite as extra transmitter is likely to have a large ephemeris error whereas one or multiple transmitters on the surface have a more predictable motion, linked to the Moon itself, which allows an accurate prediction of their positions. On the other hand, a surface transmitter can give various difficulties when considering power and thermal design due to the length of a Lunar day and night. Using the Lunar gateway (Foust [2019]) as platform for a transmitter is an interesting option for such a transmitter, especially when it is in a high altitude halo orbit. Furthermore, the option proposed by Chen et al. [2019] can be investigated as enhancements for LuNNaC, where the four cubesats in a halo orbit navigate themselves using LuNNaC, while also transmitting a navigation signal. Besides a possible enhancement in LuNNaC performance due to increased GDOP, the coverage will improve due to more signal availability at the far side of the Moon.

It is suggested that a cost-benefit analysis and conceptual design is performed for the LuNNaC system. This will map the total monetary investment required for deployment and operation of the complete system. From this, the benefits can be compared to the required investment to see if the increase in navigation performance is indeed worth the high associated investment that accompanies a satellite navigation system. A first conceptual design for the system is then needed to indicate the satellite mass, which will largely influence the launch cost, as well as the cost of required ground infrastructure needed for the operation of the system.
Related to the conceptual design of the satellites is their Delta-V budget, which needs to be assessed. Since the relative phasing of the orbits is of quite large importance for the navigation geometry, the orbit stability of the PECMEO satellites must be investigated to find the correction manoeuvres that are needed. Resulting from this, the orbit stability for various altitudes for LuNNaC could be considered in the aforementioned trade-off for orbital altitude as well.

Finally, for this research, only a few position determination methods are considered, all of which do not regard the satellite motion in their models. Therefore, it is likely that an improvement in navigation accuracy can be achieved by applying dynamic or reduced-dynamic orbit determination methods to the observation data. For this, however, the signals must be generated for a receiver orbit that is simulated with higher fidelity force models, including Lunar gravity field models.
Moreover, when considering only the kinematic positioning method, a model for the receiver clock can be introduced to link those parameters between epochs. The rather directional geometry for the navigation results in a very high correlation between radial error and receiver clock error. Using only a few estimated parameters to model the receiver clocks for all epochs could reduce this correlation, and improve the position accuracy.

Bibliography

[1] C.H. Acton. Ancillary data services of NASA's Navigation and Ancillary Information Facility. *Planetary and Space Science*, 44(1):65–70, January 1996. ISSN 0032-0633. doi: 10.1016/0032-0633(95)00107-7.

[2] V.S. Bilodeau, S. Clerc, R. Drai, and J. de Lafontaine. Optical Navigation System for Pin-Point Lunar Landing. *IFAC Proceedings Volumes*, 47(3):10535–10542, 2014. ISSN 14746670. doi: 10.3182/20140824-6-ZA-1003.01693.

[3] B. Botermann, D. Bing, C. Geppert, G. Gwinner, T.W. Hänsch, G. Huber, S. Karpuk, A. Krieger, T. Kühl, W. Nörtershäuser, C. Novotny, S. Reinhardt, R. Sánchez, D. Schwalm, T. Stöhlker, A. Wolf, and G. Saathoff. Test of Time Dilation Using Stored Li + Ions as Clocks at Relativistic Speed. *Physical Review Letters*, 113 (12):120405, September 2014. ISSN 0031-9007, 1079-7114. doi: 10.1103/PhysRevLett.113.120405.

[4] M.S. Braasch and A.J. van Dierendonck. GPS receiver architectures and measurements. *Proceedings of the IEEE*, 87(1):48–64, January 1999. ISSN 1558-2256. doi: 10.1109/5.736341.

[5] H. Chen, J. Liu, J. Long, Z. Xu, Y. Meng, and H. Zhang. Lunar far side positioning enabled by a CubeSat system deployed in an Earth-Moon halo orbit. *Advances in Space Research*, 64(1):28–41, July 2019. ISSN 02731177. doi: 10.1016/j.asr.2019.03.031.

[6] J. Christian and G. Lightsey. Review of Options for Autonomous Cislunar Navigation. *Journal of Spacecraft and Rockets*, 46(5):1023–1036, September 2009. ISSN 0022-4650, 1533-6794. doi: 10.2514/1.42819.

[7] C. D'Souza, T. Crain, F. Clark, and J. Getchius. Orion Cislunar Guidance and Navigation. In *AIAA Guidance, Navigation and Control Conference and Exhibit*, Hilton Head, South Carolina, August 2007. American Institute of Aeronautics and Astronautics. ISBN 978-1-62410-015-4. doi: 10.2514/6.2007-6681.

[8] eoPortal. Satellite Missions Directory - Earth Observation Missions - eoPortal. `https://directory.eoportal.org/web/eoportal/satellite-missions`.

[9] S.C. Fisher and K. Ghassemi. GPS IIF-the next generation. *Proceedings of the IEEE*, 87(1):24–47, January 1999. ISSN 1558-2256. doi: 10.1109/5.736340.

[10] H.F. Fliegel and R.S. DiEsposti. GPS AND RELATIVITY: AN ENGINEERING OVERVIEW. December 1996.

[11] P. Fortescue, G. Swinerd, and J. Stark. *Spacecraft Systems Engineering*. Wiley, fourth edition edition, 2011. ISBN 978-0-470-75012-4.

[12] J. Foust. Gateway or bust: NASA's plan for a 2024 lunar landing depends on a much-criticized orbital outpost. *IEEE Spectrum*, 56(7):32–37, July 2019. doi: 10.1109/MSPEC.2019.8747310.

[13] D. Hadka and P. Reed. Borg: An Auto-Adaptive Many-Objective Evolutionary Computing Framework. *Evolutionary Computation*, 21(2):231–259, May 2013. ISSN 1063-6560, 1530-9304. doi: 10.1162/EVCO_a_00075.

[14] D.G. Hoag. Apollo Navigation, Guidance, and Control Systems: A Progress Report. April 1969.

[15] G.N. Holt and B. Wood. Sextant Navigation on the International Space Station: A Human Space Exploration Demo. In *42nd Annual AAS Guidance, Navigation and Control Conference*, Breckenridge, CO, March 2019.

[16] J.J. Lissauer and I. de Pater. *Fundamental Planetary Science: Physics, Chemistry and Habitability*. Combridge University Press, 2013. ISBN 978-0-521-61855-7.

[17] M. Martin-Neira et al. PECMEO: a new space-to-space connected-element VLBI concept. In *Proceedings of the Advanced RF Sensors and Remote Sensing Instruments (ARSI'17) Workshop*. ESTEC (The Netherlands), 2017.

[18] E. Mazarico, D.D. Rowlands, G.A. Neumann, D.E. Smith, M.H. Torrence, F.G. Lemoine, and M.T. Zuber. Orbit determination of the Lunar Reconnaissance Orbiter. *Journal of Geodesy*, 86(3):193–207, March 2012. ISSN 0949-7714, 1432-1394. doi: 10.1007/s00190-011-0509-4.

[19] E. Mazarico, G. A. Neumann, M. K. Barker, S. Goossens, D. E. Smith, and M. T. Zuber. Orbit determination of the Lunar Reconnaissance Orbiter: Status after seven years. *Planetary and Space Science*, October 2017. ISSN 00320633. doi: 10.1016/j.pss.2017.10.004.

[20] E.A. Mikrin, M.V. Mikhailov, and S.N. Rozhkov. Autonomous navigation and rendezvous of spacecraft in lunar orbit. *Gyroscopy and Navigation*, 1(4):310–320, October 2010. ISSN 2075-1087, 2075-1109. doi: 10.1134/S2075108710040139.

[21] O. Montenbruck. Kinematic GPS positioning of LEO satellites using ionosphere-free single frequency measurements. *Aerospace Science and Technology*, 7(5):396–405, July 2003. ISSN 1270-9638. doi: 10.1016/S1270-9638(03)00034-8.

[22] O. Montenbruck, R. Schmid, F. Mercier, P. Steigenberger, C. Noll, R. Fatkulin, S. Kogure, and A. S. Ganeshan. GNSS satellite geometry and attitude models. *Advances in Space Research*, 56(6):1015–1029, September 2015. ISSN 0273-1177. doi: 10.1016/j.asr.2015.06.019.

[23] A. Montesano, C. Montesano, R. Caballero, M. Naranjo, F. Monjas, L.E. Cuesta, P. Zorrilla, and L. Martinez. Galileo System Navigation Antenna for Global Positioning. In *The Second European Conference on Antennas and Propagation, EuCAP 2007*, pages 1–6, November 2007. doi: 10.1049/ic.2007.1441.

[24] M.C. Moreau, P. Axelrad, J.L. Garrison, and A. Long. GPS Receiver Architecture and Expected Performance for Autonomous Navigation in High Earth Orbits. *Navigation*, 47(3):190–204, 2000. ISSN 2161-4296. doi: 10.1002/j.2161-4296.2000.tb00213.x.

[25] R. Noomen. Mission Geometry and Orbit Design: Space Mission Design, November 2017.

[26] J. S. Parker and R. L. Anderson. *Low-Energy Lunar Trajectory Design*. John Wiley & Sons, June 2014. ISBN 978-1-118-85387-0.

[27] E.M. Standish. Approximate mean ecliptic elements of the lunar orbit. 2001. doi: JPLIOM312.F-01-004.

[28] P. Steigenberger, S. Thoelert, and O. Montenbruck. GNSS satellite transmit power and its impact on orbit determination. *Journal of Geodesy*, 92(6):609–624, June 2018. ISSN 1432-1394. doi: 10.1007/s00190-017-1082-2. URL `https://doi.org/10.1007/s00190-017-1082-2`.

[29] X. Sun, P. Chen, J. Sun, and C. Han. GEO Orbit Determination Using Beidou System. September 2013.

[30] K. F. Wakker. *Fundamentals of Astrodynamics*. TU Delft, 2015.

[31] A.W. Yu, A.M. Novo-Gradaca, G.B. Shawa, and L.A. Ramos-IzquierdoC. The Lunar Orbiter Laser Altimeter (LOLA) Laser Transmitter. July 2011.

A

Universal constants and celestial properties

Table A.1: Physical constants

Symbol	Value	Quantity	Source
c	$2.997\,924\,58 \times 10^{8}\,\mathrm{m\,s^{-1}}$	Speed of light	
G	$6.674 \times 10^{-11}\,\mathrm{m^{3}\,kg^{-1}\,s^{-2}}$	Universal gravitational constant	
k	$1.380\,650 \times 10^{-23}\,\mathrm{m^{2}\,kg\,s^{-2}\,K^{-1}}$	Boltzmann constant	

Sources are respectively Acton [1996], Lissauer and de Pater [2013], and Braasch and van Dierendonck [1999].

Table A.2: Orbit and properties of the Moon

Symbol	Value	Quantity
a_m	384 400 km	Semi-major axis
e_m	0.0554	Eccentricity
i_m	5.16°	Inclination with respect to ecliptic
Ω_m	128.08°	Right ascension of the ascending node
ω_m	318.15°	Argument of periapsis
$M_{m,0}$	135.27°	Mean anomaly at $t = 0$
$\theta_{m,0}$	139.52°	True anomaly at $t = 0$
μ_m	$4.902\,720\,4 \times 10^{12}\,\mathrm{m^{3}\,s^{-2}}$	Moon gravitational parameter
R_m	1738 km	Moon radius
T_m	27d 10h	Moon orbital period

Orbital elements are from Standish [2001]. Period has been calculated using Equation C.7. Remaining parameters from Lissauer and de Pater [2013].

Table A.3: Body properties of Earth

Symbol	Value	Quantity
μ	$3.985\,979\,76 \times 10^{14}\,\mathrm{m^{3}\,s^{-2}}$	Gravitational parameter
R_E	6371.8 km	Mean Earth radius
R_E^{Eq}	6.3781×10^{6} km	Earth equatorial radius
f	1/298.257	Earth flattening

Values from Lissauer and de Pater [2013] have been used. Earth equatorial radius is calculated using Equation A.1 and Equation A.2.

$$\frac{2R^{eq} + R^{po}}{3} = R \tag{A.1}$$

$$f = \frac{a-b}{a} \tag{A.2}$$

B

Orbital parameters of LuNNaC satellites

Table B.1: The Kepler orbital elements for individual LuNNaC satellites. Inclination is defined from the ecliptic plane.

Satellite number	a [km]	e [-]	i [deg]	Ω [deg]	ω [deg]	θ [deg]
1	14000	0	88.99	318.15	0.0	0.0
2	14000	0	88.99	318.15	0.0	120.0
3	14000	0	88.99	318.15	0.0	240.0
4	14000	0	45.03	49.16	0.0	115.49
5	14000	0	45.03	49.16	0.0	235.49
6	14000	0	45.03	49.16	0.0	355.49
7	14000	0	44.98	227.14	0.0	119.99
8	14000	0	44.98	227.14	0.0	239.99
9	14000	0	44.98	227.14	0.0	359.99

C

Implementation of Kepler orbits

This appendix is dedicated to show the implementation of Kepler orbits in the navigation simulation. A division in four parts is used. Firstly, it is explained how the Kepler orbits are handled in the software, and how the orbit can be evaluated for a given time, showing the equations for finding and converting between true, mean and eccentric anomaly. Furthermore, both the routines used for coordinate transformation from Keplerian to Cartesian orbits and vice versa are shown. Finally, verification results for the Kepler orbits are shown. The majority of these methods are based on Wakker [2015].

C.1. Kepler orbits implementation and evaluation

In its essence, any defined Kepler orbit in the software consists of 7 variables. Firstly, the spacecraft state is stored as 6 Keplerian elements;

- Semi-major axis, a
- Eccentricity, e
- Inclination with respect to the ecliptic, i
- Right ascension of the ascending node, Ω
- Argument of periapsis, ω
- True anomaly at reference time t_0, θ

Moreover, the final variable is a reference to a Body object containing its gravitational parameter and a time dependent function for its Cartesian state. When an orbit around a moving body, such as a Lunar orbit, is defined, the local Cartesian state in a body fixed reference frame is superimposed on the Cartesian state of the body itself. Hence, the time dependent function for the Cartesian state of the Moon is an evaluation of its Kepler orbit, which can be found in Table A.2.

For a given elliptical Kepler orbit, the mean anomaly, M, is defined such that it increases linearly with mean motion n, given in Equation C.1.

$$n = \sqrt{\frac{\mu}{a^3}} \tag{C.1}$$

The conversion from true anomaly, θ, and mean anomaly, M, is done through the eccentric anomaly, M. The conversion from true anomaly to eccentric anomaly is shown in Equation C.2.

$$\tan\frac{\theta}{2} = \sqrt{\frac{1+e}{1-e}}\tan\frac{E}{2} \tag{C.2}$$

From this, the eccentric anomaly can be converted into mean anomaly using Equation C.3.

$$M = E - e\sin E \tag{C.3}$$

When the mean anomaly at the reference time (t_0) is found from the true anomaly at the reference time, Equation C.4 is used to find the mean anomaly at any given time t.

$$M(t) = M(t_0) + n\cdot(t - t_0) \tag{C.4}$$

Equation C.3 can not be used to directly convert the mean anomaly back to eccentric anomaly. Instead, an iterative solution is used. When the eccentricity is relatively large with $e > 0.1$, the full *Newton-Raphson method* is used, as seen in Equation C.5. As initial estimation for the first iteration $E_0 = M$ is used.

$$E_{k+1} = E_k - \frac{E_k - e\sin E_k - M}{1 - e\cos E_k} \tag{C.5}$$

For orbits with a small eccentricity, with $e \leq 0.1$, Equation C.6 is used instead. This equation is computationally less expensive, and still requires few iterations.

$$E_{k+1} = M + e\sin E_k \tag{C.6}$$

The iteration steps are continued until $|E_{k+1} - E_k| \leq 1 \times 10^{-14}$ rad. This high accuracy is needed to limit the position error to a magnitude well below the intended error sources. Meanwhile, the effect of an error in eccentric, mean or true anomaly on the Cartesian state is amplified through the orbital radius. The final step in converting back to true anomaly is done through Equation C.2.
The time taken to complete one full revolution in an orbit is the Orbital period, T, and can be calculated through Equation C.7.

$$T = 2\pi\sqrt{\frac{a^3}{\mu}} \tag{C.7}$$

C.2. Kepler to Cartesian coordinate conversion

Converting Keplerian elements to a state in Cartesian orbits start with defining the orbital radius for the given true anomaly according to Equation C.8.

$$r = \frac{a\left(1 - e^2\right)}{1 + e\cos\theta} \tag{C.8}$$

A non-rotating reference frame can be defined where the origin is located at the central body, ζ points towards perigee, and η points along the velocity at perigee. The coordinates in this frame can be calculated using Equation C.9.

$$\begin{pmatrix}\zeta\\ \eta\end{pmatrix} = \begin{pmatrix}r\cos\theta\\ r\sin\theta\end{pmatrix} \tag{C.9}$$

In order to convert these elements to the Cartesian frame, the transformation as seen in Equation C.10 is used. The elements in the transformation matrix are defined in Equation C.11.

$$\begin{pmatrix}x\\ y\\ z\end{pmatrix} = \begin{pmatrix}l_1 & l_2\\ m_1 & m_2\\ n_1 & n_2\end{pmatrix}\begin{pmatrix}\zeta\\ \eta\end{pmatrix} \tag{C.10}$$

$$\begin{aligned}
l_1 &= \cos\Omega\cos\omega - \sin\Omega\sin\omega\cos i\\
l_2 &= -\cos\Omega\sin\omega - \sin\Omega\cos\omega\cos i\\
m_1 &= \sin\Omega\cos\omega - \cos\Omega\sin\omega\cos i\\
m_2 &= -\sin\Omega\sin\omega - \cos\Omega\cos\omega\cos i\\
n_1 &= \sin\omega\sin i\\
n_2 &= \cos\omega\sin i
\end{aligned} \tag{C.11}$$

To find the Cartesian velocity components, the angular momentum of the orbit must be calculated using Equation C.12.

$$H = \sqrt{\mu a\left(1 - e^2\right)} \tag{C.12}$$

Now the individual velocity components can be calculated using Equation C.13 - C.15, using the individual transformation matrix elements as found in Equation C.11.

$$\dot{x} = \frac{\mu}{H}\left[-l_1\sin\theta + l_2\left(e + \cos\theta\right)\right] \tag{C.13}$$

$$\dot{y} = \frac{\mu}{H}\left[-m_1\sin\theta + m_2\left(e + \cos\theta\right)\right] \tag{C.14}$$

$$\dot{z} = \frac{\mu}{H}\left[-n_1\sin\theta + n_2\left(e + \cos\theta\right)\right] \tag{C.15}$$

C.3. Cartesian to Kepler coordinate conversion

From the Cartesian state of a spacecraft, the orbital radius and scalar velocity can be calculated using Equation C.16 and C.17.

$$r = \sqrt{x^2 + y^2 + z^2} \tag{C.16}$$

$$V = \sqrt{\dot{x}^2 + \dot{y}^2 + \dot{z}^2} \tag{C.17}$$

The semi-major axis of the Kepler orbit can be found using Equation C.18.

$$a = \frac{1}{\frac{2}{r} - \frac{V^2}{\mu}} \tag{C.18}$$

The eccentricity vector of the orbit is found using Equation C.19. From this, the scalar eccentricity is found from the magnitude of the eccentricity vector; $e = |\vec{e}|$.

$$\vec{e} = \frac{\vec{V} \times \vec{h}}{\mu} - \frac{\vec{r}}{r} \tag{C.19}$$

In order to find the remaining parameters, the angular momentum vector, $\vec{H}$, is calculated using Equation C.20. Here, H_x, H_y, and H_z are the vector components along respectively x, y, and z axes.

$$\vec{H} = \begin{pmatrix} H_x \\ H_y \\ H_z \end{pmatrix} = \begin{pmatrix} x \\ y \\ z \end{pmatrix} \times \begin{pmatrix} \dot{x} \\ \dot{y} \\ \dot{z} \end{pmatrix} \tag{C.20}$$

From this, the inclination is calculated using Equation C.21.

$$i = \arccos \frac{H_z}{|\vec{H}|} \tag{C.21}$$

Moreover, the equations in Equation C.22 yield an unambiguous solution for the right ascension of the ascending node, Ω.

$$\sin\Omega = \frac{H_x}{\sqrt{H_x^2 + H_y^2}}; \quad \cos\Omega = \frac{-H_y}{\sqrt{H_x^2 + H_y^2}} \tag{C.22}$$

The argument of periapsis is calculated through Equation C.24, where its sign is found through Equation C.25. The vector $\hat{\vec{N}}$ is the unit vector of vector $\vec{N}$, defined in Equation C.23.

$$\vec{N} = \begin{pmatrix} 0 \\ 0 \\ 1 \end{pmatrix} \times \vec{H} \tag{C.23}$$

$$\omega = sign_\omega \cdot \arccos\left(\hat{\vec{e}} \cdot \hat{\vec{N}}\right) \tag{C.24}$$

$$sign_\omega = \begin{cases} +1, \text{if} \left(\hat{\vec{N}} \times \vec{e}\right) \cdot \vec{H} > 0 \\ -1, \text{otherwise} \end{cases} \tag{C.25}$$

Finally, the true anomaly is calculated through Equation C.26, the sign of which is calculated using Equation C.27.

$$\theta = sign_\theta \cdot \arccos\left(\hat{\vec{r}} \cdot \hat{\vec{e}}\right) \tag{C.26}$$

$$sign_\theta = \begin{cases} +1, \text{if} (\vec{e} \times \vec{r}) \cdot \vec{H} > 0 \\ -1, \text{otherwise} \end{cases} \tag{C.27}$$

C.4. Verification of Kepler orbit implementation

Several steps have been taken in order to verify the Julia implementation. Firstly, the coordinate transformation from Kepler to Cartesian, and vice versa are verified through example cases from Noomen [2017]. The Keplerian elements for these cases are shown in Table C.1 and the corresponding Cartesian coordinates are in Table C.2. The gravitational parameter for these conversions is given as $\mu = 398\,600.441 \times 10^9\,\mathrm{m^3\,s^{-2}}$.

Table C.1: Keplerian elements for two example orbits.

Element	Orbit 1	Orbit 2
a [m]	6787746.891	7096137.00
e [-]	0.000731104	0.0011219
i [°]	51.68714486	92.0316
Ω [°]	127.5486706	296.1384
ω [°]	74.21987137	120.6878
θ [°]	24.10027677	239.54374
E [°]	24.08317766	239.5991
M [°]	24.06608426	239.6546

Table C.2: Cartesian elements for two example orbits.

Element	Orbit 1	Orbit 2
x [m]	-2700816.14	3126974.99
y [m]	-3314092.80	-6374445.74
z [m]	5266346.42	28673.59
V_x[m s^{-1}]	5168.606550	-254.91197
V_y[m s^{-1}]	-5597.546618	-83.30107
V_z[m s^{-1}]	-868.878445	7485.70674

After converting these Cartesian orbits to their Kepler equivalent, the elements are compared to the correct values according to the original data. The difference in Keplerian elements is shown in Table C.3. Furthermore, this table also shows the errors in conversion from true anomaly to eccentric anomaly to Mean anomaly, and finally, the back-conversion to true anomaly. It can be observed that most errors are in the order of magnitude of the least significant digit of the original data, or lower.
A similar comparison has been performed for the conversion from Keplerian elements to Cartesian coordinates. The differences between the calculated parameters and the original data is shown in Table C.4. This conversion has been performed using the original true anomaly as starting point. Once again, the magnitude of the offset between values is around the least significant digit in the original data, and thus is to be expected.

Table C.3: Errors in orbital elements after converting example Cartesian states to Kepler orbits.

Element	Orbit 1	Orbit 2
Δa [m]	-7.348×10^{-7}	1.469×10^{-2}
Δe [-]	1.289×10^{-10}	-9.930×10^{-10}
Δi [°]	4.299×10^{-10}	-3.025×10^{-8}
$\Delta\Omega$ [°]	-2.493×10^{-8}	1.941×10^{-8}
$\Delta\omega$ [°]	1.851×10^{-9}	-4.657×10^{-5}
$\Delta\theta$ [°]	6.935×10^{-8}	4.658×10^{-5}
ΔE [°]	-3.017×10^{-10}	1.045×10^{-4}
ΔM [°]	-1.275×10^{-9}	4.654×10^{-5}
$\Delta\theta$ [°] (back conversion)	-6.461×10^{-10}	7.827×10^{-5}

Besides coordinate transformations, the implementation of orbit propagation, or assessment of Keplerian elements at a given time, must be verified as well. This is performed by taking the orbit corresponding to *Orbit 1* in Table C.1 and comparing the initial true anomaly to that assessed at a time of one orbital period

Table C.4: Spacecraft state error after converting orbits described in Kepler elements into Cartesian states.

Element	Orbit 1	Orbit 2
x [m]	-4.589×10^{-3}	-4.538×10^{-3}
y [m]	4.563×10^{-3}	3.949×10^{-3}
z [m]	1.545×10^{-3}	-2.436×10^{-3}
V_x [m s^{-1}]	-1.799×10^{-6}	-3.693×10^{-6}
V_y [m s^{-1}]	-1.544×10^{-6}	-1.264×10^{-6}
V_z [m s^{-1}]	7.188×10^{-6}	-2.041×10^{-6}

later, calculated using Equation C.7. For a perfect orbit assessment, the orbital phase should be identical after exactly one orbital period. The corresponding orbital period is 5565.44 s, and an error in true anomaly of $\Delta\theta = -1.25 \times 10^{-15}$° is observed. Similarly, the mean anomaly after one quarter period should be progressed by 90°, while this progression is different for the true anomaly due to the eccentricity of the orbit. The error for the mean anomaly $M(0) + 90° - M(T/4) = -3.88 \times 10^{-15}$°. Meanwhile the true anomaly progresses by 90.042° in this time, which is clearly different from 90°, as is expected.
For *Orbit 2*, from Table C.1, an orbital period of 5949.0 s is found. The error in true anomaly when assessing after one orbital period is -3.27×10^{-18}°. The offset in mean anomaly after quarter period, from the expected 90°, is -3.48×10^{-15}°.

D

Software dependencies

For this research project, the following software has been used.

- Julia programming language[1] 1.2
- Atom[2] 1.41.0 x64
- MATLAB 2019a

The following non-standard packages for the Julia language, have been used.

- BlackBoxOptim.jl[3] v0.5.0
- Plots.jl[4] v0.27.0
- DoubleFloats.jl[5] v0.9.13
- ProgressMeter.jl[6] 1.2.0

The source code for the simulations written for this thesis can be found at:

`https://github.com/maGriffioen/pecmeoNav`

[1] `https://julialang.org/`
[2] `https://atom.io/`
[3] `https://github.com/robertfeldt/BlackBoxOptim.jl`
[4] `https://github.com/JuliaPlots/Plots.jl`
[5] `https://github.com/JuliaMath/DoubleFloats.jl`
[6] `https://github.com/timholy/ProgressMeter.jl`


TUDelft